

### Public Domain Mark 1.0 Universal

This work was written as part of one of the author's official duties as an Employee of the United States Government and is therefore a work of the United States Government. In accordance with 17 U.S.C. 105, no copyright protection is available for such works under U.S. Law.

Access to this work was provided by the University of Maryland, Baltimore County (UMBC) ScholarWorks@UMBC digital repository on the Maryland Shared Open Access (MD-SOAR) platform.

### **Please provide feedback**

Please support the ScholarWorks@UMBC repository by emailing [scholarworks-group@umbc.edu](mailto:scholarworks-group@umbc.edu) and telling us what having access to this work means to you and why it's important to you. Thank you.

# JGR Atmospheres

## RESEARCH ARTICLE

10.1029/2023JD039085

### Key Points:

- Remote-sensed imagery of smoke plumes at different spatial and temporal resolutions are used to observe smoke magnitude and dispersion near fire sources
- High-resolution, sub-orbital imagery helps quantify limitations of lower-resolution orbiting sensors for observing smoke's magnitude and evolution
- Satellite products with spatial resolution less than the width of the plume can capture the mean but not the maximum smoke loading

### Supporting Information:

Supporting Information may be found in the online version of this article.

### Correspondence to:

Y. R. Shi,  
[yingxi.shi@nasa.gov](mailto:yingxi.shi@nasa.gov)

### Citation:

Shi, Y. R., Levy, R. C., Remer, L. A., Mattoo, S., & Arnold, G. T. (2024). Investigating the spatial and temporal limitations for remote sensing of wildfire smoke using satellite and airborne imagers during FIREX-AQ. *Journal of Geophysical Research: Atmospheres*, 129, e2023JD039085. <https://doi.org/10.1029/2023JD039085>

Received 15 APR 2023

Accepted 18 DEC 2023

### Author Contributions:

**Conceptualization:** Y. R. Shi, R. C. Levy, L. A. Remer

**Data curation:** S. Mattoo, G. T. Arnold

**Formal analysis:** Y. R. Shi

**Funding acquisition:** R. C. Levy

**Investigation:** Y. R. Shi

**Methodology:** Y. R. Shi, R. C. Levy, L. A. Remer

**Project Administration:** R. C. Levy

**Resources:** R. C. Levy

**Supervision:** R. C. Levy, L. A. Remer

**Validation:** Y. R. Shi

**Visualization:** Y. R. Shi

**Writing – original draft:** Y. R. Shi

**Writing – review & editing:** Y. R. Shi, R. C. Levy, L. A. Remer

## Investigating the Spatial and Temporal Limitations for Remote Sensing of Wildfire Smoke Using Satellite and Airborne Imagers During FIREX-AQ

Y. R. Shi<sup>1,2,3</sup> , R. C. Levy<sup>2</sup> , L. A. Remer<sup>1,3</sup>, S. Mattoo<sup>2,4</sup>, and G. T. Arnold<sup>2,4</sup>

<sup>1</sup>Goddard Earth Sciences Technology and Research II, Baltimore, MD, USA, <sup>2</sup>NASA Goddard Space Flight Center, Greenbelt, MD, USA, <sup>3</sup>University of Maryland Baltimore County, Baltimore, MD, USA, <sup>4</sup>Science Systems and Applications, Inc., Lanham, MD, USA

**Abstract** Starting from point sources, wildfire smoke is important in the global aerosol system. The ability to characterize smoke near-source is key to modeling smoke dispersion and predicting air quality. With hemispheric views and 10-min refresh, imagers in Geostationary (GEO) orbit have advantages monitoring smoke over once-per-day sensors in low-earth orbit (LEO). However, both can be inadequate in capturing the characteristics of smoke plumes close to their sources due to too-coarse spatial resolution (both detector and product resolution), too-sparse temporal resolution (from LEO sensors), and too-conservative masking. In addition to satellite observations, the Fire Influence on Regional to Global Environments and Air Quality experiment offered sub-orbital enhanced-MODIS Airborne Simulator (eMAS) imagery at 50 m pixel resolution—including multiple eMAS flight tracks over individual fires in short time periods. It provided opportunity to explore smoke plume characterization at various spatial and temporal scales and quantify the limitations of space sensors for describing smoke magnitude near source as well as its temporal evolution. Here we applied modified aerosol algorithm to different imagers, relaxing its masking to estimate smoke's aerosol optical depth (AOD) as close as possible to its source. We found that GEO sensors with nominal 1 km spatial resolution can match the much finer resolution eMAS retrieved mean plume AOD, as long as the retrieval spatial resolution is finer than the width of the plumes. However, the plume's maximum AOD may be drastically underestimated by satellite products.

**Plain Language Summary** Starting from point sources, wildfire smoke is important in the global aerosol system. The ability to characterize smoke near-source is key to modeling smoke dispersion and predicting air quality. Satellite-based sensors provide important information about smoke plumes, however, by themselves can be inadequate in capturing the characteristics of smoke plumes close to their sources. In addition to geostationary orbit (GEO) satellite observations with 1–2 km spatial resolution observations at 10-min intervals and low-earth orbit (LEO) at 0.5–1 km resolution observations daily, the Fire Influence on Regional to Global Environments and Air Quality (FIREX-AQ) experiment offered sub-orbital (airborne) enhanced-MODIS Airborne Simulator (eMAS) imagery at 50 m pixel resolution. With multiple eMAS flight tracks over individual fires in short time periods, FIREX-AQ provided opportunity to explore smoke plume characterization at various spatial and temporal scales and quantify the limitations of space sensors for describing smoke magnitude near source as well as its temporal evolution. Here we applied a modified aerosol algorithm to all the different imagers, relaxing its masking to estimate smoke's aerosol optical depth (AOD) as close as possible to its source. We found that GEO sensors with nominal 1 km spatial resolution can match the much finer resolution eMAS retrieved mean plume AOD, as long as the retrieval spatial resolution is finer than the width of the plumes. However, the plume's maximum AOD may be drastically underestimated by satellite products.

## 1. Introduction

Most aerosol types, far from their sources, can be described as relatively homogeneous hazes and palls, at least on the order of 30–100 km. Therefore, satellite observations on the order of ~3–10 km are generally sufficient to characterize the climatology (Anderson et al., 2004; Shinozuka & Redemann, 2011). For 20 years, the two MODerate resolution Imaging Spectroradiometers (MODIS) on the Terra and Aqua satellites, have been making such observations of the global aerosol system and deriving a long-term data record of key aerosol products

(Gupta et al., 2016; Levy et al., 2010, 2013; Remer et al., 2005). These data products, such as aerosol optical depth (AOD), Fine Mode Fraction and Ångström Exponent (AE) have provided unique characterization and insight into distribution and change of aerosol loading across the globe and have been used in many aerosols related studies (Chin et al., 2014; Ichoku et al., 2003; Koren et al., 2010; Manoj et al., 2011; Ramanathan et al., 2007; Van Donkelaar et al., 2015; Yu et al., 2008, 2020; Yuan et al., 2011). These MODIS aerosol products are available at two spatial resolutions of 3 and 10 km at nadir, twice daily, which is adequate for providing a rough estimate of daily global aerosol distribution. Likewise, once-per-day observations are adequate to discern long-range transport of these palls during their multiday lifetimes (Hodzic et al., 2016; Kaufman et al., 1992, 2003; Kristiansen et al., 2016). Thus, the decades of AOD data derived from MODIS have made important contributions to their designed science and applications purposes, namely characterization of aerosol on global, regional, and climatological scales.

Close to aerosol sources, the traditional polar-orbiting satellite sensors such as MODIS and their retrieval products have demonstrated limitations. In particular, rapidly evolving smoke plumes from individual wildfires defy the conventions defined by typical aerosol palls. These smoke plumes vary at much finer spatial and temporal scales, spewing smoke aerosol from fire sources that can be only a few tens of meters in size, and changing minute by minute (Ortega et al., 2013; Reid et al., 2005; Yokelson et al., 2009). Small fire (with size <10 km) occurs frequently. The SCAR-B (Kaufman, Hobbs, et al., 1998) campaign shows that fires with average size around 0.01 km<sup>2</sup> occur most frequently and the number fires decreases exponentially as the fire size increases in log scale (Kaufman, Kleidman, & King, 1998). Though starting from small point sources, wildfire smoke plays a key role in the global aerosol system. Smoke particles evolve quickly from their source and can eventually homogenize into smoke palls that can cover continental areas, as they age and are transported downwind. Thus, smoke can modify clouds over large regions and can be a major source of air pollution for millions of individuals. The ability to characterize smoke at the source is key to understanding and modeling smoke dispersion and air quality forecasting.

There are three reasons that traditional satellite aerosol products have been inadequate in capturing the characteristics of wildfire smoke plumes close to their sources, including (a) coarse spatial resolution, (b) coarse temporal resolution and (c) aggressive masking (e.g., mis-labeled clouds) by the algorithm. In the following, we will describe these factors in more details using MODIS Dark Target (DT) aerosol products and algorithm as an example.

The first major limitation of MODIS-like products is spatial resolution. While wildfires can cover vast areas, the majority (98% or more) are much smaller, typically less than 4 km<sup>2</sup> in extent (<https://sgp.fas.org/crs/misc/IF10244.pdf>). Consequently, most fires remain smaller than the spatial resolution of a standard-product MODIS AOD retrieval (10 km<sup>2</sup>). Furthermore, the fire front is often only a few meters across, smaller than the finest pixel resolution of the MODIS sensor (250 m). Thus, wildfire smoke is generated at spatial scales considerably finer than the satellite sensor's resolution, and the resulting plume may not meet thresholds for detectability and then retrieval by a particular sensor (Roberts et al., 2009; San-Miguel-Ayanz & Ravail, 2005; Wang et al., 2018). In order to observe these fine-resolution fires and resulting smoke plumes, we need an imaging sensor with enhanced spatial resolution.

Not only do smoke plumes originate over small areas, but they also evolve quickly. The traditional polar-orbiting satellite sensors with their once-per-day sampling of wildfire regions cannot resolve the temporal characteristics of individual smoke plumes (Freeborn et al., 2011; Wang et al., 2018; Wiggins et al., 2020; Williamson et al., 2012). At best they might accumulate ensemble characteristics of these plumes over many fire seasons. Even so, diurnal biases might skew the ensemble statistics to provide incomplete or biased understanding of near-source smoke (Lennartson et al., 2018; Liu & Zeng, 2019). Since 2015, a new generation of geosynchronous satellite sensors have enhanced spatial and spectral capabilities to allow aerosol retrieval using similar algorithms as used for MODIS. The advantage of these sensors, including the Advanced Himawari Imager (AHI) and the Advanced Baseline Imagers (ABIs), is that they provide full disk (hemispheric) images every 10 min instead of twice per day (Schmit et al., 2005). The disadvantages compared to MODIS include fewer wavelength bands and coarser spatial resolution (e.g., 2 km common) for aerosol retrieval (Schmit et al., 2018). As part of this study, we will evaluate ABI's temporal advantages versus its limited spatial resolution.

The third issue for the standard MODIS retrieval algorithm is aggressive cloud and scene masking. Aerosol algorithms are tuned to find scenes that match their inherent assumptions (Remer et al., 2005). For example, the DT

aerosol algorithm applied to MODIS and other sensors is designed to retrieve over dark cloud-free, snow-free, glint-free ocean and land scenes. Pixels that are designated as clouds, ice/snow, glint, and bright land scenes, are therefore “masked” out using tests designed to find these scenes. For example, over land the algorithm is looking for dark vegetation, but not inland water or swamps. Because fresh smoke plumes can be both “bright” and “lumpy”-looking, they can resemble clouds in a spatial sense and non-vegetated surfaces in a spectral sense. Therefore, the DT algorithm may mask out these smoke plumes and no retrieval is made (Brennan et al., 2005; Remer et al., 2012; Y. R. Shi et al., 2019). We can force the algorithm to retrieve these fresh smoke plumes but doing so opens the algorithm to cloud contamination and poor retrievals for other scenes around the globe.

The Fire Influence on Regional to Global Environments Experiment-Air Quality (FIREX\_AQ, Warneke et al., 2023) campaign offers opportunities to assess the ability of satellite aerosol products in quantifying smoke plumes near their source regions. The campaign was held in the United States from July to August and October to November 2019. The primary objective of FIREX-AQ was to quantify fire emissions and investigate their correlation with various factors such as fuel type, burning conditions, emission transport, dispersion, evolution, and air quality impact. As part of its mission, FIREX-AQ aimed to establish a connection between wildfire data sets retrieved from satellites and ground measurements by utilizing airborne measurements and imagery. Our interest here is related to the observations from enhanced-MODIS airborne simulator (eMAS), which by flying at 20 km altitude, is akin to MODIS or ABI, yet with much finer spatial resolution (50 m vs. 0.5–2 km).

By using high-resolution eMAS data we aim to answer this key question: Can satellite aerosol retrievals effectively provide meaningful characterization of smoke plumes near emission sources, considering their constrained spatial and temporal capabilities? Since this study is limited to the FIREX-AQ domain (Western U.S. during late summer 2019), we can modify (relax) the masking so that the algorithm would retrieve in cases that a standard algorithm would avoid (Y. R. Shi, Levy, Yang, et al., 2021). By allowing adequate retrieval in the small domain, we can focus on the specific questions about the spatial and temporal resolution of smoke, rather than the decision to retrieve or not to retrieve. The caveat is that we cannot generally apply this relaxed masking to the global algorithm.

In the next section we describe the data sets that are used to answer the question, and their status as standard products. Section 3 describes validation of the eMAS DT standard product against Aerosol Robotic Network (AERONET) and intercomparison of the different AOD products from different sensors. Although there are some biases and discrepancies, there is sufficient agreement among the sensors to proceed with our investigations regarding higher spatial and temporal resolutions, along with relaxed cloud and scene masks. This leads to “smoke-focused” and “experimental” algorithms described in Section 4, which are applied to eMAS and ABI data that force the retrieval of aerosol plumes. Section 5 provides a comprehensive examination of how the spatial resolution impact the representation of smoke plume near the source using satellite aerosol products. In Section 6 we present the findings of the temporal resolution study. Finally, in Section 7, we answer the question of whether spatial and temporal limitations prevent meaningful characterization of near-source aerosol wildfire plumes.

## 2. Data

### 2.1. Generic DT Algorithm and Products

A passive remote sensing imager, such as MODIS, observes reflectance or radiance in multiple visible, near-infrared (NIR), shortwave-infrared (SWIR) and terrestrial infrared (TIR) wavelength bands. Each band is an image with pixels at a specific spatial resolution (may be different between bands). When geo-located (associated with latitude/longitudes on the surface, as well as observing geometry), we denote the set of spectral, native-resolution observations as the Level 1B (L1B) data.

From a subset of the L1B data, the DT algorithm was developed to retrieve aerosol properties, including AOD over land and ocean separately at 0.55  $\mu\text{m}$ , as well as in other bands. Since we are focusing on smoke in the Western U.S., we focus on the land portion. In general, the standard DT algorithm does the following: (a) aggregate  $N \times N$  worth of native-resolution pixels into retrieval boxes. (b) “mask” pixels which do not conform to the algorithm's assumptions (e.g., ice/snow surfaces, ephemeral water, bright surfaces), (c) Perform a statistical filtering that removes 20% of the darkest and 50% of the brightest pixels, (d) from the remaining pixels, perform some small corrections for gas-absorption, and calculate mean reflectance in each band, (e) compare the mean Top-Of-Atmosphere (TOA) reflectance to lookup tables (LUTs) of pre-calculated reflectance of “typical”

aerosol scenes, (f) retrieve AOD and other properties, and (g) assign quality assurance and confidence (QAC) to the retrievals. Note that to perform (e) “the retrieval,” the DT algorithm assumes a relationship between surface reflectance at three wavelength bands (nominally blue, red, and a SWIR band near 2.1 or 2.2  $\mu\text{m}$ ), which constrains the surface contribution to the TOA.

Here explains the key masks within (b) that matters to this study in the standard DT over land algorithm:

- Inland water mask: based on calculating Normalized Vegetation Difference Index (NDVI), which is the ratio of the sum and difference of the observed reflectance in the red and NIR bands. This test is a powerful test that can remove many surface conditions that are not suitable for the DT retrieval algorithm. Values less than 0.01 suggest thin layers of water on the Earth's surface, including melting snow, slush, or swamp surfaces.
- Cloud masks: two cloud masks are used. One for thin cirrus clouds and one for low clouds. Both cloud masks are threshold-based tests on both reflectance and standard deviation of the reflectance. The thin cirrus cloud mask utilizes near-infrared water vapor bands ( $\sim 1.38 \mu\text{m}$ ), and the low cloud mask uses blue channel. In the standard algorithm the two thresholds for low cloud mask are 0.4 and 0.0025 for reflectance and standard deviation of reflectance respectively. The low cloud mask ensures that only homogeneous features will be retrieved, and the feature needs to have “not so bright” appearance.

Details of the DT operational over land algorithm (as applied to MODIS) are presented in Remer et al. (2005) and Levy et al. (2010) and Levy et al. (2013). These procedures guarantee a robust DT aerosol global distribution. Modifications to the standard algorithm are required for use on eMAS and ABI because of differences in wavelength or spatial resolution.

### 2.1.1. MODIS Standard Products

MODIS sensors onboard the Terra and Aqua satellites each provide Earth observations, in 36 spectral wavelength bands, once per day during daylight hours. Depending on band, observations have nominal resolutions of 250 m, 500 m or 1 km, where Bands 1–7 are at 500 m or better and we denote as (blue = 0.47  $\mu\text{m}$ , green = 0.55  $\mu\text{m}$ , red = 0.65  $\mu\text{m}$ , NIR = 0.86  $\mu\text{m}$ , SWIR1 = 1.24  $\mu\text{m}$ , SWIR2 = 1.64  $\mu\text{m}$ , and SWIR3 = 2.11  $\mu\text{m}$ ). The over-land aerosol retrieval relies directly on three of these bands (blue, red and SWIR3), and indirectly on the SWIR1 (for constraining land surface reflectance via the 2.11/1.24 NDVI<sub>swir</sub>) (Levy et al., 2013). Cloud, inland-water and ice/snow masking requires additional bands including the NIR, SWIR2, the 1 km cirrus/water vapor absorption band at 1.38  $\mu\text{m}$  and selected 1 km resolution bands in the TIR. The result is that DT algorithms provide MODIS aerosol products twice per day at 10 and 3 km spatial resolution (Gupta et al., 2018; Levy et al., 2010, 2013). Note that since the nominal native-resolution of most bands used in the DT algorithm is 0.5 km, the retrieval uses a  $6 \times 6$  aggregation (the 3 km) or a  $20 \times 20$  aggregation (the 10 km) before masking and statistical filtering.

The DT algorithm is well established based on the MODIS sensor and the DT MODIS product has been widely tested, validated, and used in many studies (Gupta et al., 2016; Levy et al., 2010, 2013; Y. Shi et al., 2011). A quality assurance (QA) number is assigned to each retrieved AOD based on retrieving conditions. The “very good” quality data (QA = 3) is recommended to use for quantitative study of aerosols. The expected error envelope (EE) is an error threshold of which 67% of the “very good” quality data falls within when compared against ground-based measurements. For overland MODIS C6 product, EE for AOD at 0.55  $\mu\text{m}$  is  $\pm (0.05 + 15\%)$  of AERONET AOD (Levy et al., 2013). Although the temporal coverage of MODIS DT product is not as ideal, we still use MODIS DT product in this study as we have high confidence in MODIS DT AOD where ground based AOD measurement is not available.

### 2.1.2. DT Applied to Geostationary ABI

The DT algorithm can be applied to other sensors that have similar spectrum structures including VIIRS on Suomi-NPP and NOAA-20/JPSS1, AHI on Himawari-8, and ABI on GOES-16 and GOES-17. Among these sensors, we use mainly observations from ABI, which is better positioned to observe our study region in the western US. ABI-16 and ABI-17 provide high temporal observation in 16 spectral bands with nominal 2 km, 1 km, and 500 m resolution. Note that although there are ABI images with higher time resolution (the CONUS views at 5 min and the MESO views at 1 min), we are using the Full Disk (hemispheric) images taken every 10 min (<https://www.goes-r.gov/users/abiScanModeInfo.html>). Although all satellites experience an enlarged pixel size at the edge of their field of view (FOV) (Peterson et al., 2013), a geostationary (GEO) sensors' pixel size increase is worse due to its higher orbit altitude. ABI-17 and ABI-16 both observe the FIREX\_AQ domain, however



ABI-17's location (at the GOES-West position of  $-137^\circ$  longitude) provides a more direct view (smaller pixel size) than ABI-16's location (at the GOES-East position of  $-75^\circ$ ). The static viewing zenith angle looking at our study region are around  $58^\circ$  from ABI-17 and around  $69^\circ$  from ABI-16, which means 2 versus 5 km instead of nominal 1 km resolution observations. One issue might be that the shorter atmospheric path length in ABI-17 compared to ABI-16 (GOES-R Series Data Book) means reduced signal to noise, however, this is not a concern due to the strong signal of smoke plume.

There are some differences between ABI and MODIS/VIIRS sensors that impact consistent application of the DT algorithm, including fewer wavelengths and coarser spatial resolution. To accommodate these differences, a "DT-package" toolset has been developed to consistently retrieve AOD over multi-platform sensors. For ABI, there is no  $0.55\ \mu\text{m}$  (or equivalent green band), nor a  $1.24\ \mu\text{m}$  (or equivalent SWIR1 band). Without a green band, the over-ocean retrieval may be degraded slightly, but there is no impact on the over-land retrieval. Without the SWIR1 band, DT-package compensates by using other wavelength bands. These accommodations include substituting the  $0.86\ \mu\text{m}$  NIR for the  $1.24\ \mu\text{m}$  over land for estimates of NDVI\_SWIR and using the  $1.64\ \mu\text{m}$  band for masking snow/ice (Huang et al., 2018).

While ABI's equivalent blue = 0.47, red = 0.64, NIR = 0.86, and SWIR2 =  $1.64\ \mu\text{m}$  bands have a nominal resolution of 1 km or better, the equivalent SWIR3 band at  $2.25\ \mu\text{m}$  band has resolution of 2 km. To make the most use of the higher resolution observations, the  $2.25\ \mu\text{m}$  is interpolated to 1 km. At the same time, we have recognized that all sensors (MODIS, VIIRS and ABI/AHI) have a red band (e.g.,  $0.64\text{--}0.67\ \mu\text{m}$  depending on sensor) that has the highest spatial resolution (e.g., MODIS = 250 m, VIIRS = 375 m, ABI/AHI = 500 m), so that the cloud masking spatial variability test is revised to use this red band. Initial studies (in preparation) show that the DT-Package modifications applied to MODIS do not significantly impact overall product quality—(canceling minor improvements/degradations), so when used with GEO data, it could be expected to have similar characteristics. Initial studies using AHI data (Gupta et al., 2019) show overall reasonable quality of AOD retrievals from a GEO sensor, however with a high bias (possibly due to missing  $1.38\ \mu\text{m}$  cirrus band and/or calibration biases, Bruegge et al., 2021). With ABI, we expect to see similar characteristics. An initial version of a standard DT-ABI product will soon be available (Y. Shi, Levy, Remer, et al., 2021), with retrievals of AOD and other parameters at nominal  $10\ \text{km} \times 10\ \text{km}$  resolution (e.g.,  $10 \times 10$  aggregations of the common 1 km resolution pixels).

Here we focus on the ABI (16 and 17) retrievals over the FIREX-AQ domain, including "standard" ABI products ( $10 \times 10$  resolution from the DT-Package), and two modified ABI products that are "smoke focused" and "experimental" to highlight the smoke plumes in the region. Section 4 in detail explained the differences between "smoke focused"/"experimental" algorithm and the standard DT algorithm. These modifications mainly include relaxation of cloud and inland water masks (to focus on the smoke), introducing new cloud mask using NIR channels, and testing different pixel aggregations ( $N \times N$ ) to look at the retrievals.

### 2.1.3. DT Suborbital Product on eMAS

Providing a "bridge" of spatial resolution between satellite retrieved fire emission data and ground-based measurements, airborne eMAS imagery captured intricate details of small-scale smoke plumes between 22 July and 19 August 2019. On specific days (e.g., 6–8 August), eMAS conducted multiple flyovers of a particular fire (the William's Flat fire, Ye et al., 2021; Junghenn Noyes et al., 2020; Kumar et al., 2022) within a brief interval, yielding MODIS-like products with exceptionally high temporal/spatial resolution. These data enable an evaluation of satellite aerosol products' capacity to characterize small-scale smoke plumes.

eMAS is a multispectral sensor with 19 bands very close to MODIS channels, including the ones that the algorithm uses to retrieve aerosols. The difference is that from high-altitude aircraft ( $\sim 20\ \text{km}$ ), eMAS provides a 37 km wide swath and 50-m spatial resolution in all bands. Therefore, DT can be applied to eMAS with only minor changes. The first is that  $1.88\ \mu\text{m}$  is substituted for  $1.38\ \mu\text{m}$  for cirrus detection. With no  $1.24\ \mu\text{m}$  band, the  $0.86\ \mu\text{m}$  is substituted for an NDVI\_swir—similar to what is used for ABI. The result is an eMAS aerosol retrieval using  $10 \times 10$  eMAS pixels which is approximately  $\sim 0.5\ \text{km}$  resolution at nadir. More details about the standard DT-algorithm for eMAS can be found in Spencer et al. (2019). Note that LUT and other boundary conditions were updated for the exact wavelength bands (Bruegge et al., 2021).

The DT algorithm is applied to all eMAS data during the FIREX\_AQ campaign. General validation of the DT eMAS product is presented in Section 3 against AERONET and other DT satellite products. On board the ER-2 from Armstrong (Dryden) Flight Research Center (AFRC), eMAS sensor observed multiple wildfires emitting

**Table 1**  
Comparing Standard Enhanced-MODIS Airborne Simulator (eMAS) Products With

Sensor	Time window (min)	Space window	Min # of eMAS retrievals
AERONET	30	6 km	5
MODIS Terra/Aqua 10 km	30	All eMAS retrievals within each satellite footprint	30
MODIS Terra/Aqua 3 km	30		5
ABI (GOES-16 and GOES-17)	5		50

smoke plumes during the FIREX\_AQ campaign, among which the Williams Flat fire (6–8 August 2019) is well observed and used in this study.

Between 6–8 August 2019, eMAS flew over the Williams Flat fire multiple times within a short period. Although with different views (combinations of solar and view angles as well as along the plume or across the plume), there are continuous sampling of the smoke plume including a total of 7 tracks on 6 August, 7 tracks on 7 August, and 5 tracks on 8 August 2019. We highlight these flights (e.g., 6 August) in our comparisons in Section 6, combined with ABI product to study the temporal evolution.

Similarly, as performed for ABI, we will study both standard-eMAS products, “smoke focused,” and “experimental” eMAS products that highlight the smoke (by modifying spectral/spatial tests, as well as the  $N \times N$  resolution). The standard eMAS products are available via LAADS DAAC website ([https://ladsweb.modaps.eosdis.nasa.gov/archive/MAS\\_eMAS/FIREXAQ/](https://ladsweb.modaps.eosdis.nasa.gov/archive/MAS_eMAS/FIREXAQ/)).

## 2.2. The Aerosol Robotic Network (AERONET)

Ground truth in this study come from two types of AERONET sites deployed for the FIREX\_AQ campaign, “fixed” sites and “mobile” sites. The mobile sun photometer was deployed attaching to a car (Sano et al., 2016). In fact, for some cases they roughly followed the eMAS flight tracks. AERONET direct sun measurements provide AOD that has well-characterized uncertainties of 0.01 in the visible and 0.02 at ultraviolet (UV) wavelengths (Eck et al., 1999). Collocation data set between AERONET observed AOD and eMAS DT AOD are generated with spatial and temporal differences set to be 6 km and 30 min, respectively. A sensitivity study was conducted by varying the spatial and temporal collocation criteria (not shown here). We found that increasing the spatial collocation range will increase the scatter of the collocation data set significantly while shortening the time window does not change the overall error statistics. Thus, to ensure enough samples in the data set, we selected this set of collocation criteria. AERONET does not provide AOD observations at 0.55  $\mu\text{m}$ . Thus, interpolation of AOD at 0.55  $\mu\text{m}$  from AODs at 0.40–1.02  $\mu\text{m}$  is done according to a best fit polynomial (N. T. O’Neil et al., 2001, 2003). The AERONET data level 1.5 from permanent sites and lev1.0 from mobile sites are used in this study to ensure data volumes, especially for mobile sites. Mobile 1 site recorded some AOD greater than 0.8 during the field campaign in level 1.0 data, however, these collocated high AOD data points were removed in level 1.5. Thus, we use two different levels of AERONET data to validate the eMAS DT product during FIREX\_AQ campaign. Also note that although the high AOD value observed by mobile\_1 AERONET is around 1.0–1.2, it is still not at the center of the smoke plume (personal communication with Dave Giles) where most of the missing DT AOD occurs (see Figure 4c).

## 3. Validation and Intercomparisons of Standard DT eMAS AOD Data With Other Aerosol Products

Here, we begin by adopting MODIS-like thresholds for cloud masking, pixel selection, etc., and apply to the eMAS observations during FIREX-AQ. This we denote as the “standard” eMAS DT product. These products are compared with AERONET, standard MODIS 3 km products, and standard ABI-17 products. Note different temporal and spatial windows based on the expected information content of each sensor. Table 1 shows the collocation criteria that are used to collocate eMAS and other data sets as well as the minimum number of eMAS retrievals required before averaging into one value to be compared. All thresholds are selected via sensitivity study to ensure a robust error statistic while maintain the largest amount of paired data available for validation.

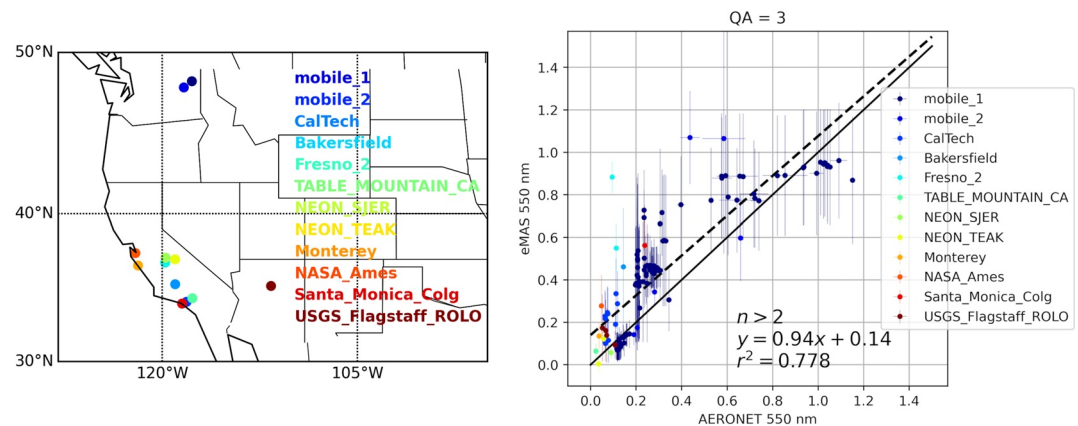


**Figure 1.** Map of Aerosol Robotic Network (AERONET) sites used in the validation (left) and validation of enhanced-MODIS Airborne Simulator (eMAS) against AERONET lev1.5 permanent sites and lev1.0 mobile site data set (right). The standard deviation of the averages in both AERONET and eMAS Dark Target (DT) aerosol optical depth data are shown. Color represents sites. Only collocated datapoints with at least two AERONET data available within the averaging period is displayed. Only the best quality over land eMAS DT data are used.

### 3.1. DT eMAS Validated Against AERONET

Figure 1 shows the comparison of the eMAS standard DT product with AERONET, with different colored dots representing the different AERONET sites (both fixed and mobile). The standard deviation of averaged data from both AERONET (temporal average) and eMAS (spatial average) are shown by error bars. Overall, eMAS retrievals agree well with AERONET observations. Note that at low AOD ( $AOD < 0.2$ ), the eMAS collocations with mobile\_1 data almost falls on the 1 to 1 line. Because the mobile sites purposely follow the eMAS track, this set of collocation data have minimum spatial/temporal sampling differences. The takeaway message is that eMAS AOD matches AERONET AOD to within the spatial standard deviation of the retrievals within the collocation.

### 3.2. DT eMAS Compared With Other DT Satellite Products

Intercomparisons between DT products from eMAS and MODIS onboard Terra/Aqua (both 10 and 3 km), and ABI-16/17 onboard GOES-East/West are also performed. As an example, Figure 2 focuses on the William's Flat Fire, comparing AOD retrieved from two eMAS flight tracks on 6 and 7 August 2019, along with the DT eMAS AOD overlaying on MODIS Aqua AOD, and AOD images of MODIS Aqua, ABI-16, and 17. On 7 August 2018, the top row of Figure 2, all three satellite products show very similar AOD patterns, all generally agreeing with eMAS but having a much coarser resolution. Due to its location at 75°W, ABI-E views the fire at the edge of its full disk and has coarser pixel resolution than ABI-W. The pixel size of the MODIS product varies by view angle in each granule. Although the general pattern/magnitude of AOD between all four products is similar, there are differences in AOD. These differences in AOD arise partially from sampling/algorithm differences attributed to individual sensors, but also partially due to temporal changes in the smoke itself. The lower row of Figure 2 shows 6 August 2019, where eMAS and MODIS Aqua observed elevated smoke AOD, while both ABI 16 and 17 have trouble capturing the smoke. Compared to the emission pattern in Figure 2a, the plume in Figure 2f is much finer in spatial extent.

Quantitative comparisons between the eMAS, MODIS, and ABI products, for all FIREX-AQ campaign flights are shown in Figure 3. Due to the nature of very fine spatial resolution of eMAS DT product, comparisons of MODIS 3-km DT products and eMAS products are shown in Figure 3 instead of the standard 10-km MODIS DT products. The error statistics and overall comparisons between the MODIS 10-km product and eMAS is very similar to what we see with the MODIS 3-km product, just with fewer datapoints. This shows that when not focusing on individual fire emission, satellite AOD products robustly represent background aerosol loading regardless of spatial resolutions. However, these comparisons only show results when both sensors produce a retrieval, but do not show what satellite retrievals are missing. All eMAS retrievals that have observation times within 30 min of MODIS' overpass time or within 5 min of ABI's observing time, and are located within the satellite retrieval footprint, are averaged for the collocation comparison. The time differences of 5 min between



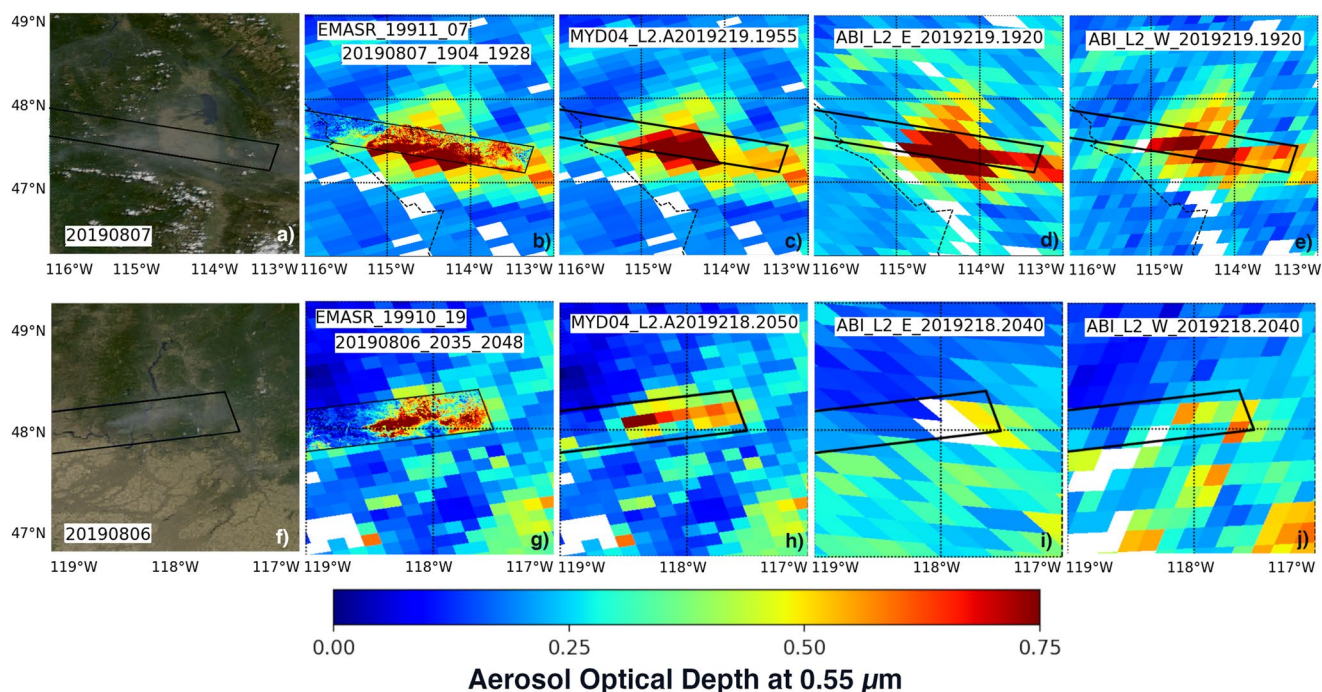


**Figure 2.** Williams flat fire on 7 August (top row) and 6 August (bottom row) 2019 with collocated enhanced-MODIS Airborne Simulator (eMAS) and satellite imagery and aerosol optical depth (AOD) products. From left to right: RGB image from Aqua MODIS with outline of the collocated eMAS swath on the image; AOD product from eMAS overlaid onto an image of AOD product from Aqua MODIS; AOD product from Aqua MODIS without the eMAS AOD overlay; AOD from ABI-East; AOD from ABI-West. The eMAS track time and satellite passing time are listed in each image. The outline of the eMAS swath appears in each satellite image.

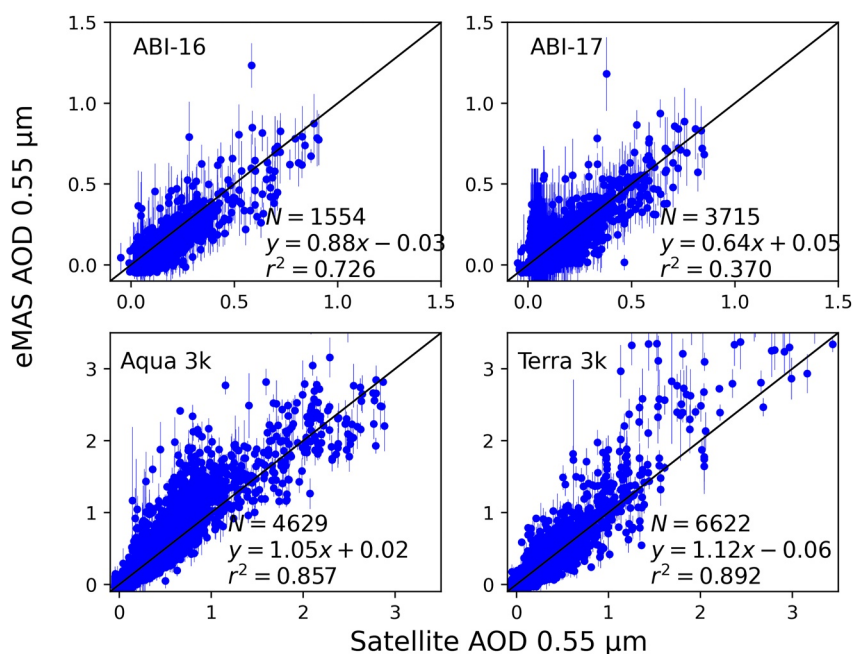


**Figure 3.** Intercomparisons between enhanced-MODIS Airborne Simulator and MODIS/Advanced Baseline Imager Dark Target (DT) products. MODIS Aqua/Terra and ABI-16/17 products are shown with error statistics plotted. Only the best quality over-land DT data are used.

**Table 2**

*Error Statistics From Comparisons Between Dark Target (DT) Enhanced-MODIS Airborne Simulator (eMAS) Products and DT Products on MODIS and Advanced Baseline Imager (ABI) Sensors During the FIREX\_AQ Period*

eMAS versus	Median bias	RMSE	Slope	R	% Within EE	#
MODIS Aqua 10 K (MYD)	0.011	0.0081	1.09	0.92	70	528
MODIS Terra 10 K (MOD)	−0.027	0.0056	1.17	0.93	70	870
MODIS Aqua 3 K	−0.002	0.0030	1.09	0.92	65	4,629
MODIS Terra 3 K	−0.015	0.0019	1.12	0.93	65	6,622
ABI-W	−0.0008	0.0017	0.64	0.61	50	3,715
ABI-E	−0.048	0.0022	0.88	0.85	61	1,554

*Note.* The Median Bias is eMAS minus other DT products.

eMAS and ABI guarantee that no multiple ABI snapshots will be collocated to the same set of eMAS retrievals. Due to the different temporal collocation criteria between collocating with MODIS and ABI, the collocated retrievals can have sampling differences. Because an eMAS flight track can be 20–30 min long, having a 5-min collocation window, only partial flight tracks are collocated with one ABI time frame, leaving the rest of the track collocated with different ABI scans. With MODIS, if the MODIS granule covers the entire spatial extent of the eMAS flight track, all eMAS retrievals will be collocated to this one MODIS granule, divided into individual MODIS retrieval boxes. The spatial size of the satellite retrieval footprint also impacts collocation. MODIS and ABI retrieval size are both 10 km at nadir; however, this size can be much larger toward the edge of the satellite FOV (Peterson et al., 2013), where ABI will have a much coarser retrieval size than MODIS. Aiming to reduce sampling bias when ABI retrievals are located at the edge of the FOV, extra filtering is applied. We require at least 50 eMAS data points in the satellite footprint and the standard deviation of averaged eMAS needs to be less than 0.25. This filter ensures that enough eMAS retrievals fall within the ABI retrieval box so that the eMAS observation is representative of the whole retrieval box. Note the thresholds on standard deviation also will remove some ABI retrievals which are partially covered by a smoke plume. Thus, the comparisons in Figure 3 aim toward understanding algorithm performance for general conditions (background aerosol loading). Analyses of satellite product performance for smoke plumes are discussed in Sections 5 and 6.

Figure 3 shows that, in general, the eMAS DT product aligns closely with all four satellite products with most of the paired AOD data following the one-to-one line. From the slope statistics, the eMAS DT retrieval shows slightly higher from MODIS and slightly lower than ABI. However, some of these slope values are driven by outliers. They may not mean that eMAS/satellite data are biased low or high, but rather differences exist between them. Later in the paper, we show that the satellite can have a large underestimation of AOD when a fine-scale smoke plume exists. The magnitude of the underestimation depends on the plume size. Thus, the less than one slope for ABI-17 is mainly caused by high eMAS AODs when satellite AOD < 0.5, and the larger than one slope in MODIS is caused by high eMAS AODs when satellite AOD > 1.5, both high and low biases result from sampling issues when operational satellites must resolve small scale smoke plumes. Note that MODIS Aqua is chosen to be our satellite “standard” due to its well validated AOD products (Gupta et al., 2018; Hyer et al., 2011; Levy et al., 2018). As Figure 3 shows that eMAS AOD retrievals are closer to those from Aqua than ABI, we will bring ABI AOD closer to eMAS AOD in Section 5 and 6, where we discuss the representativeness of retrieved AOD from ABI and eMAS. Table 2 lists all the statistics of comparisons between DT eMAS products and DT products on MODIS and ABI sensors. Overall, the DT eMAS AOD compares well with the DT products on MODIS and shows a slightly low bias when compared with DT AOD on ABI.

Although statistics can show the bulk performance of the DT products, a case study better illustrates how eMAS DT AODs align with satellite retrievals over small smoke plumes. Looking back at Figure 2, we see that ABI sensors miss the smoke plume on 6 August. Why? Is this something inherent in the sensors' capabilities, which will forever prevent monitoring small smoke plumes with confidence? Is this a spatial resolution issue or a temporal resolution issue? Can we define spatial and temporal parameters to assure better characterization of small smoke plumes? To answer these questions, we will modify the global standard DT algorithm to better capture small smoke plumes and use the modified algorithm to investigate the relationship between the smoke spatial and temporal characteristics and the ability of satellites to retrieve these emissions.

**Table 3**  
*Descriptions of Three Dark Target Algorithm Used in This Study*

	Standard DT	Smoke focused	Experimental
Purpose	Global	Retrieve smoke plume with conservative masking	Only used for spatial analyses; retrieves as much AOD as possible
Used in	Section 3 Validation	Section 6 Temporal analyses	Section 5 Spatial analyses
Spatial resolution	10 km (ABI) 500 m (eMAS)	3 km (ABI) 500 m (eMAS)	Various for both eMAS and ABI
Shallow cloud mask	Threshold of the standard deviation of reflectance of blue channel is 0.0025	Threshold changes to 0.005 Addition of NIR parameter from MOD06 <sup>a</sup>	Threshold changes to 0.0075
NDVI	Threshold of inland water mask is 0.1	Threshold changes to 0.01	Same as smoke focused
Data prefilter	20% darkest 50% brightest pixels are removed	Same with standard DT algorithm	10% darkest and 5% brightest pixels are removed

<sup>a</sup>Only applied to eMAS but not ABI.

#### 4. Smoke-Focused and Experimental Algorithm

The standard DT algorithm is designed to maximize the algorithm's global potential at the expense of sometimes losing the ability to fully characterize specific local aerosol phenomena. Small smoke plumes are one of the local aerosol situations that challenge the standard global algorithm. The purpose of this study is to define the inherent limitations of the satellite sensor, not necessarily the algorithm, when confronted with smoke plumes of small spatial extent and short time scales. To meet this purpose, we develop a family of DT algorithms tuned to the local, not global situation, including a smoke focused algorithm, and an experimental algorithm. The description and usage of the algorithm in this paper is listed in Table 3 and is explained in detail in this section. These algorithms are applied to eMAS and ABI, making modifications to the retrieval box size (varying the  $N \times N$  of native pixels), the cloud and inland water filters, and the pixel filtering (modifying the percentage of darkest and brightest pixels discarded before averaging the reflectance).

Figure 4 is an example of eMAS DT AOD retrieval using the three different algorithms. Figure 4c shows an example of how the standard DT algorithm applied to eMAS observations misses the center of the plume on 8 August 2019 (Flight #19912, Track #09), during the Williams Flat fire. The RGB image (Figure 4a) show that on top of the track, thick smoke exists with puffy clouds embedded inside smoke. The standard DT eMAS AOD covers large areas of the plume with AOD as high as 3.5 but still misses an area with the optically thick smoke. Both the cloud mask (Figure 4b) and the inland water masks contribute to the missing coverage in general, however for this specific flight track, the missing coverage is due to the inland water mask.

To increase the coverage, several changes are made to the data preprocessing procedures (Y. R. Shi et al., 2019; Y. Shi, Levy, Remer, et al., 2021; Y. R. Shi, Levy, Yang, et al., 2021), including cloud mask and inland water mask. The cloud mask is modified with two steps. First, additional metrics that utilize near-infrared and infrared wavelengths (1.6, 2.1, and 3.7  $\mu\text{m}$ ) to separate cloud and aerosols based on their particle size differences (Platnick et al., 2003) is introduced to include optically thick smoke plumes which were previously removed by standard shallow cloud masks using only the blue (e.g., 0.47- $\mu\text{m}$ ) channel. This metric is a product of the MODIS-VIIRS cloud optical properties algorithm (Platnick et al., 2003) and beyond the scope of the DT group to produce. It is available in the eMAS cloud product but is not yet available on ABI. Thus, this change is only applied on eMAS. Second, the thresholds in the shallow cloud mask (Martins et al., 2002), which separates clouds and aerosols by examining the variability and brightness of a feature, are also relaxed. Specifically, the threshold of the standard deviation within a  $3 \times 3$  sample of pixels and the threshold on the reflectance value in the blue band are adjusted based on Table 3. The inland-water mask is also modified. Although the NDVI test is a powerful test that can remove thin layers of water, or other surface conditions that are not suitable for the DT retrieval algorithm, it can also remove situations where the surface is obscured by optically thick aerosol. Thus, the conservative thresholds of inland water mask are relaxed. The details of these changes are described in Y. R. Shi et al. (2019), Y. Shi, Levy, Remer, et al. (2021), Y. R. Shi, Levy, Yang, et al. (2021). All above-mentioned changes are adapted in the smoke-focused algorithm. Figure 4d shows that the smoke focused DT algorithm retrieves significantly more data within the plume, while still being able to identify embedded clouds when compared to the standard algorithm.



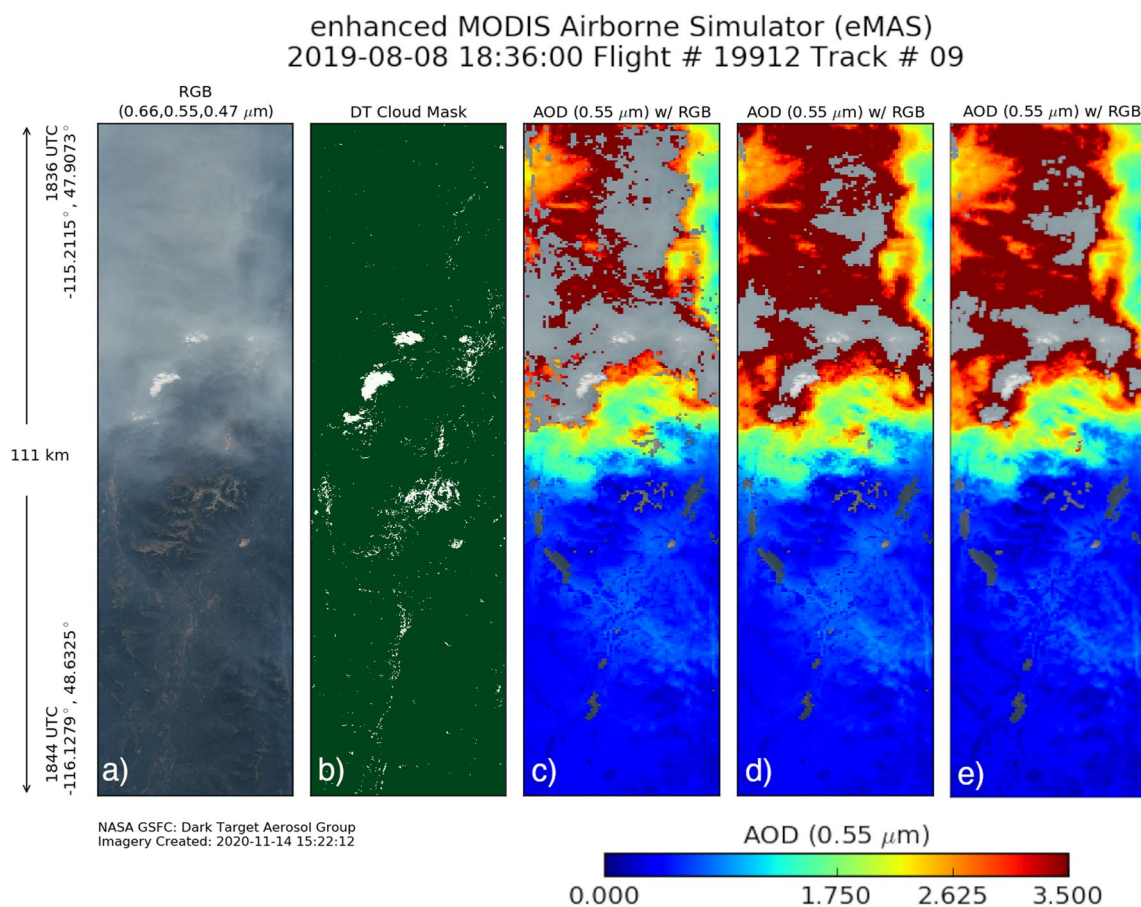


**Figure 4.** One enhanced-MODIS Airborne Simulator flight track on 9 August 2019, Flight number 19912 and track number 09. From left to right: the RGB image (a), the Dark Target (DT) cloud mask with white indicating clouds and dark green indicating cloud-free (b), DT aerosol optical depth at 0.55  $\mu\text{m}$  from the standard algorithm (c), the smoke-focused algorithm (d), and experimental algorithm (e).

For the experimental algorithm, further adjustment is made to the data prefiltering step, which happens after the masking procedures. The motivation for the experimental algorithm is that after applying the smoke focused algorithm on ABI data, we still miss a significant number of retrievals within the plume region at certain retrieval box sizes. This causes a problem when testing the spatial resolution impact on retrieved plume AOD. Thus, the experimental algorithm is designed to specifically work on ABI data and is only used during spatial analysis investigations. The standard DT algorithm removes 50% of the brightest and 20% of the darkest pixels in each aggregated retrieval box. This statistical filtering is intended to remove cloud shadows and high reflectance surface noise under the assumption that aerosol homogeneously covers the entire retrieval box. However, small scale smoke plumes cause large spatial variation in AOD within a small region, which is contrary to the assumption that the aerosol is homogeneous. This is especially problematic when the plume only covers a small fraction of the retrieval box. Therefore, to recover even smaller plumes, we can adjust the pixel filtering process to exclude only 5% of the brightest pixels and 10% of the darkest pixels. Again, this change will cause artifacts if the brightest feature within the retrieval box is not a smoke plume. Thus, this algorithm is only used for demonstrating the impact of spatial resolution (Section 5). Note that while the brightest/darkest filter is intended to eliminate non-aerosol characteristics, we are aware that the standard filtering along with the aggregation method chosen can introduce a slight low bias in the retrieved AOD under circumstances where the retrieval box contains aerosols devoid of subgrid clouds or cloud/topographic shadows (Sayer & Knobelspiesse, 2019). By changing the filter that negative bias may be mitigated. As long as we keep same filtering/aggregation procedures throughout our spatial analyses (Section 5), the bias exist is consistent. The experimental eMAS AOD in Figure 4e shows wider data coverage in the smoke-focused algorithm (Figure 4d). Note that Figures 4d and 4e are both at eMAS standard 500-m resolution, with the smoke plume able to fill most of each retrieval box. Therefore, the differences between smoke focused and experimental versions of the algorithm will only show slight differences. At coarser

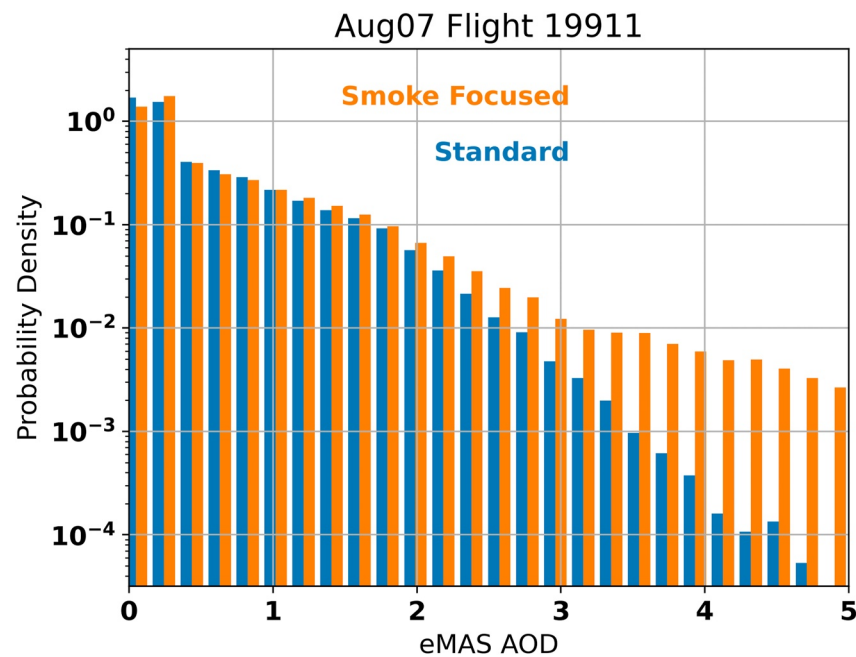


**Figure 5.** Enhanced-MODIS Airborne Simulator Dark Target (DT) aerosol optical depth (AOD) distributions on 7 August 2019, flight 19,911 between standard (blue) and research (orange) products. Note that the research algorithm produces many more retrievals at high AOD but does not decrease the number of pixels at moderate or low AOD, as compared with the standard DT algorithm.

ABI resolution where plumes only partially fill retrieval boxes, the differences between the smoke focused and experimental algorithms will display greater significance.

To show statistically how the smoke focused algorithm differs from the standard algorithm, we apply the smoke focused algorithm to another eMAS track, 7 August 2019, flight track 19,911, during the second day of the Williams Flat fire. This is the track with the highest AODs retrieved from the entire eMAS deployment. Here we do not include the experimental algorithm because for eMAS the smoke focused, and experimental algorithms do not show significant statistical differences. Figure 5 demonstrates the increase in the number of retrievals with AOD magnitude greater than 3 using the smoke focused algorithm from that of the standard algorithm. Similar plots of AOD distributions are investigated for all eMAS flight tracks that observe smoke plumes. Large increase in high AOD data volume is seen for all of them.

## 5. Understanding Spatial Resolution and Aggregation Impacts on Retrievals

There are two spatial resolutions at work here. First, there is the native spatial resolution of the sensor. Second, there is the DT aggregation algorithm that determines the spatial resolution of the product. A native pixel represents the size of the sensors' observation, say of reflectance in a given wavelength band. In the case of eMAS it is nominally 0.05 km, for ABI it is 1 km at nadir. One can aggregate those native pixels into a box, say  $N \times N$  of those pixels. Within that  $N \times N$  retrieval box, the standard DT algorithm masks, and filters, and calculates a mean reflectance from the subset of native pixels that are suitable for retrieval. Our experimental algorithm follows the same concept, except there is less masking. Thus, because of the pre-filtering procedures, the reported AOD does not represent the average aerosol status within the retrieval box, but rather the aerosol status of a subset within the box that is suitable for retrieval. If the aerosol is homogeneous across the retrieval box, as is the case for most aerosol hazes, then there is no issue with the method. However, with small smoke plumes the aerosol is inhomogeneous so that the aggregate spatial resolution and pixel selection make significant difference to characterization of a scene. Here we discuss spatial resolution of the retrieval box or how the pixels are grouped for retrieval and not the resolution of the sensor itself.

AOD products from ABI and eMAS were aggregated into various  $N \times N$  retrieval box resolutions to answer spatial resolution related questions. By systematically varying  $N$ , variable AOD resolutions are generated for ABI



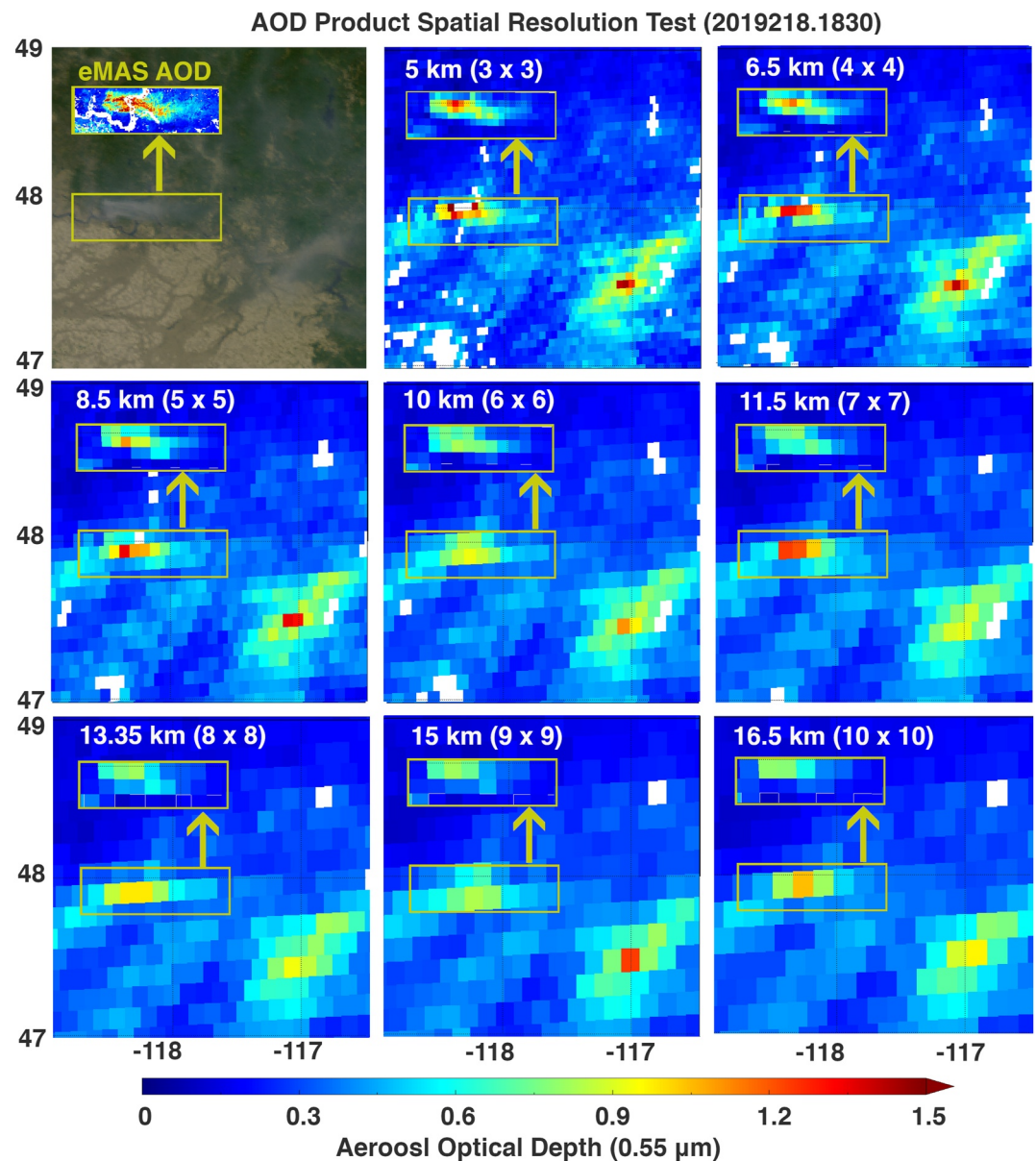


**Figure 6.** Series ABI-17 Dark Target aerosol optical depth (AOD) image at Williams flat fire on 6 August 2019, 18:30 UTC, with changing product pixel size. The AOD size changes from averaging of 5 km (3 by 3) level1b pixels to 16.5 km (10 by 10) pixels. The RGB image of Advanced Baseline Imager is shown with a box identifying the enhanced-MODIS Airborne Simulator (eMAS) swath in yellow outline and also an inset of the eMAS AOD superimposed onto an empty section of the RGB image.

and eMAS AOD retrievals. ABI AOD retrieval boxes varied from  $N = 3$  to  $N = 10$ . Because of the spreading of the ABI native pixels away from the sub-satellite position at the equator, this creates variable ABI AOD spatial resolution spanning 5–16.5 km. eMAS AOD resolutions varied from  $N = 3$  to  $N = 300$ , creating eMAS retrieval box sizes 0.15–15 km.

Figure 6 shows an example of how spatial resolution of the retrieval box impacts the satellite product representing a smoke plume. It shows an ABI-W granule on 6 August 2019, 18:30 UTC (2019218.1830) with a corresponding eMAS track between 18:34 to 18:46 UTC. The ABI AOD retrieval box size changes with  $N$  values ranging between 3 and 12, increased by 1. The corresponding eMAS AOD with similar retrieval box size is also overplotted on top of the ABI AOD. Note that although ABI data has 1 km level1B spatial resolution at nadir, due to the location of the plume within the full disk image, the retrieval box size is larger than  $1 \times N$  km. The corresponding

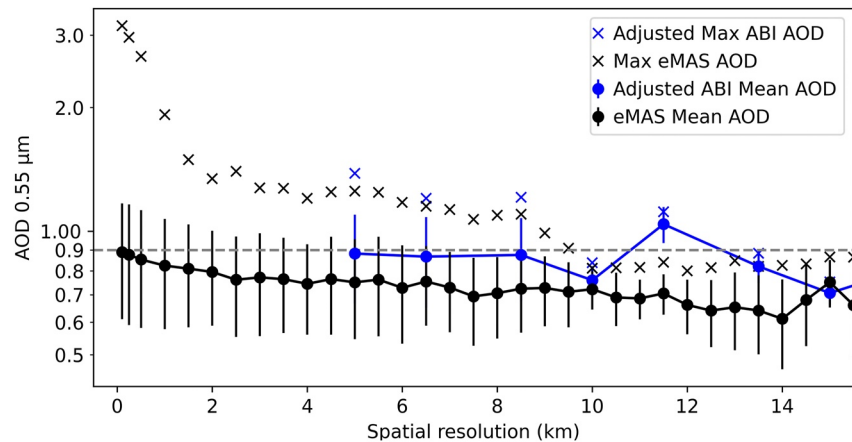


**Figure 7.** Advanced Baseline Imager (ABI) and enhanced-MODIS Airborne Simulator (eMAS) Dark Target research product plume aerosol optical depth (AOD) as function of retrieval box spatial resolution at Williams Flat Fire on 6 August 2019. ABI data is at 18:30 UTC and eMAS is flight track #8 from 18:34 to 18:46 UTC. The dots and lines are the mean and standard deviation of plume AOD from ABI/eMAS as function of retrieval box sizes in km. The crosses are the maximum AOD in the defined plume. The blue and black are ABI and eMAS data, respectively. Note that ABI AOD were adjusted with 10% reduction to compensate the AOD differences between ABI and eMAS based on Figure 2.

retrieval box size in km is listed in parentheses. Because of the space limitation, only AOD images with  $N$  less than 11 are shown in Figure 6.

There are some caveats in Figure 6: (a) ABI covers much larger area than eMAS swath, thus can include more background pixels when retrieval box becomes very large at the edge of the eMAS swath. (b) Even for the same AOD resolution, ABI and eMAS have different averaged TOA reflectance values because of the sensors differences in native pixel resolution. (c) the eMAS flight track is along the smoke plume, which aligns the eMAS pixels parallel to the smoke plume direction. ABI scan lines are not parallel. This means that the percentage of smoke within each retrieval box varies along an ABI row. The image loses the spatial continuity of the plume. Next, we take a detailed look at how retrieval box size impacts the AOD retrieval and is dependent on the shape of the target plume and its environment.

The smoke plume from the Williams Flat fire is transported eastwards, starting at around  $118.5^{\circ}\text{W}$  and  $48^{\circ}\text{N}$ . The direction of the plume is slightly toward the southeast, which is opposite of the ABI-17 scan line that angles slightly toward the northeast. The plume has a clear-cut linear northern boundary and a relatively clean but slightly curved southern boundary. The larger the  $N$ , the wider the retrieval box becomes, and the representation of the plume changes. One might assume that the finest resolution, the  $5\text{ km}$  (corresponding to  $3 \times 3$  pixel aggregation) AOD image, would produce a plume that most closely resembles the very fine resolution eMAS image. The problem is that the sharp boundary at the northern edge of the plume creates a large variation of top-of-atmosphere reflectance within the  $3 \times 3$  grid that spans this boundary. This triggers the spatial variability cloud mask, and we lose three retrievals right where the smoke is thickest. These appear as white squares in the  $3 \times 3$  panel of Figure 7. However, to the west and east of these three grid boxes, depending on how much smoke is within the defined retrieval box, AOD retrievals are successful. The magnitude of retrieved AOD is approximately 1.5, which is similar to the averaged plume AOD eMAS reports, but much lower than the peak AOD eMAS retrieves. The row of retrieval boxes to the south of the three empty boxes is partially filled with plume, all grid points are retrieved successfully but reported with lower AOD than eMAS. This low bias of satellite AOD is also visible at the very beginning of the plume close to the emission source. Depending on the variation of the plume intensity and the relative location of the plume within the grid-box, optically thick plume signals can be diluted by non-plume pixels, leaving retrieved AOD much lower than reality. No missing AOD retrievals of the plume are noted for the rest of the  $N$  values. However, the value of retrieved AOD varies depending on the designated box size. As one would assume, when the spatial resolution gets coarser, the contribution of the smoke plume lessens relative to the whole grid box, resulting in lower AOD values.

When compared to the eMAS AOD with similar sized retrieval box that is overplotted on top of the ABI AOD image, the ABI AOD is surprisingly similar to the magnitude of the eMAS AOD, if not higher. Note that the

**Table 4**

*Statistics of Defined Smoke Plume on Enhanced-MODIS Airborne Simulator (eMAS) Including the Mean Plume Width, Standard Deviation (StdDev) of the Plume Width, Mean eMAS Plume Aerosol Optical Depth (AOD), and AOD Threshold Used in Defining the Plume Width*

eMAS time	Mean plume width (km)	StdDev of plume width	Mean eMAS plume AOD	AOD threshold
18:34–18:46	5.35	3.23	0.97	0.62

ABI AOD is systematically slightly higher than eMAS AOD in Section 3 (Figure 3; Table 2). But overall, we see similarities between the ABI and eMAS retrieved smoke plume and its surrounding AOD when the retrieval box sizes are small (e.g., 5 km retrieval box resolution). This spatial similarity reduces when the retrieval box gets bigger especially when ABI AOD shows much larger fluctuation of AOD depending on the retrieval box size. It's the combination of changing retrieval box size and the pixels selected after filtering procedures that creates these differences.

In the above exercise we explored the consequences of using different retrieval box resolutions from the same satellite sensor to characterize a small smoke plume and presented the results spatially to illustrate the interplay between grid and plume location. We next provide a more quantitative analysis. We will present two parameters for characterization of the smoke plume. The first is the average AOD of the plume. The second is the maximum retrieved AOD within the plume. We will calculate these parameters using the same smoke plume of the Williams Flat Fire on 6 August 2019, that we presented in Figure 6. Here we apply the DT smoke-focused algorithm with various retrieval box sizes to the ABI scan at 18:30 UTC and the corresponding eMAS flight track (number 08, time from 18:34 to 18:46). We compare the two parameters of the coarse resolution ABI aerosol retrieval with that of the much finer resolution eMAS AOD to estimate inherent biases in satellite AOD due to coarse spatial resolution and how those changes as retrieval box size changes.

To calculate our two metrics: average plume AOD and maximum AOD within the plume, we must first define the plume. Plume regions are selected based on AOD values. A small rectangular area (Lat: 47.9–48.05 N, Lon: 118.2–118.9 W) is drawn to include the extent of the plume as observed from the union of all ABI AOD DT products, covering the five times of ABI observation. Plume identification is further refined by excluding AOD boxes lower than a dynamic threshold. The threshold is defined as the mean AOD within the rectangle plus 0.3 of the standard deviation of the AOD. Thus, the plume is defined as all pixels within the rectangle that have slightly higher than mean AOD. This practice is applied to both ABI and eMAS retrieved AOD and the AOD cutoff is calculated for each data set. The calculated AOD cutoff values are 0.5–0.7 for ABI, which are reasonable when compared to what is shown in Figure 6. The influence of varying AOD thresholds on eMAS and ABI plume statistics was tested. We found no impact to our conclusions from choosing a slightly higher or lower AOD cutoff value.

Once the plume is defined the width of the plume can be calculated using eMAS data. Table 4 shows the statistics of the defined smoke plume. Due to the east-west orientation of the plume, the plume width here is simply defined as the distance between the far north point of the plume to the far south point, assuming 74 km per degree latitude at 48°N. The plume direction changes slightly based on wind directions between 18:10 to 18:40, tilting the plume slightly toward northeast or southeast, which impacts the calculated plume width. The nature of the downwind dispersal of smoke also impacts the mean plume width as well as the standard deviation of the plume width. Based on the plume statistics and the RGB image of the plume time evolution, the mean plume width is approximately 5–7 km.

After the spatial extent of the plume is defined, the two metrics: mean AOD of the plume and maximum AOD of the plume can be calculated for the ABI and eMAS data, for a variety of retrieval box spatial resolutions. Figure 7 shows these results with mean plume AOD in dots and maximum AOD in crosses. ABI and eMAS plume statistics are shown in blue and black, respectively. Due to known AOD systematic differences between ABI and eMAS data, in order to bring ABI and eMAS retrievals together at the same magnitude, a 10% reduction were implemented to ABI mean and maximum AOD.

Figure 7 shows that at the finest ABI retrieval box at 5 km (3 × 3), the mean plume AOD from ABI is very close to adjusted mean AOD from the smallest eMAS retrieval box (50-m), which are both around 0.9. Mean eMAS plume AOD decreases almost linearly as retrieval box size increases. The slope of this decrease is around −0.012 AOD per km when retrieval box size is larger (>2 km). The mean ABI plume AOD remains constant as retrieval boxes change as long as the spatial resolution is finer or comparable to the plume width. When retrieval box size exceeds plume width, the mean ABI plume AOD fluctuates as ABI rows align and misalign with the plume axis, as seen in Figure 6. This implies that at certain spatial resolutions, the satellite-retrieved mean plume AOD can be very unpredictable/unstable. If the retrieval boxes continue to grow beyond this range of instability to be much

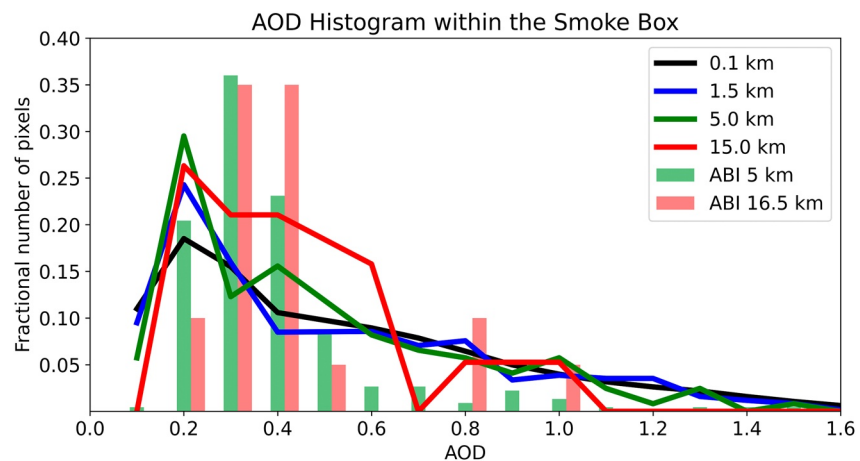


**Figure 8.** Aerosol optical depth histogram of Advanced Baseline Imager (ABI) Dark Target (DT) research and enhanced-MODIS Airborne Simulator (eMAS) DT research data under various retrieval box sizes. ABI is from 6 August 2019, 18:30 UTC and eMAS is flight track #8 from 18:34 to 18:46 UTC over defined smoke region 47.9°–48.05°N and 118.2°–118.9°W. The fractional number of data are shown with eMAS data in lines and ABI data in bars.

larger than the width of the plume, the retrieval box will always encapsulate the plume. At that point increasing the retrieval box further acts to dilute the mean plume AOD with background AOD. Mean plume AOD then monotonically decreases with increased dilution.

Although mean plume AOD from ABI is comparable to eMAS mean plume AOD at fine resolution, the maximum ABI AOD is much lower than those at 50 m resolution. The maximum AOD decreases sharply with increase of retrieval box size when spatial resolution is less than 2.0 km (slope of  $-1.2$  AOD per km) and then decreases slowly beyond 2.0 km resolution (slope of  $-0.04$  AOD per km). The plume maximum AOD at finest eMAS retrieval box resolution is around AOD of 3, while that number is halved for ABI retrievals. Above 5 km resolution, where both ABI and eMAS report retrievals, unexpectedly ABI maximum plume AOD is higher than eMAS'. The explanation has been traced back to the filtering procedures on eMAS, where the fine resolution isolates the brightest input reflectance pixels corresponding to maximum plume AOD to just a few pixels that are eliminated during the algorithm masking process. Even though these filtering procedures have been modified for the experimental algorithm used here (Table 3), they still find the isolated maximum input values and remove them from processing. ABI's coarser native resolution smooths over the isolated maximums, which prevents their elimination. The result is that despite having the same size retrieval box, eMAS and ABI are reporting different maximum AOD that have undergone different filtering experiences because of differences in native pixel size.

The analyses using mean and maximum plume AOD provide straightforward results of how satellite pixel size impact the plume statistics. However, simply using mean and maximum AOD cannot answer how spatial resolution of satellite products impact the AOD distribution of the plume. Thus, we analyzed AOD histograms within a fixed box (48.05°–47.9°N, 118.2°–118.9°W) that contains the plume to understand whether the AOD distributions are similar between the eMAS retrieved AOD under various retrieval box resolution and between those from ABI retrievals. We selected eMAS retrieval box spatial resolution of 0.1, 1.5, 5.0, and 15 km and corresponding ABI 5 km ( $3 \times 3$ ) and 16.5 km ( $10 \times 10$ ) retrievals. The normalized number of pixels within every 0.1 AOD bin is plotted to have fair comparisons under vast differences of data volumes between these data. This histogram cuts off at AOD of 1.6, beyond that the AOD distribution has very few numbers and is not shown here. The eMAS statistics are shown in lines while ABI is plotted in bars. Figure 8 shows that although ABI has similar mean plume AODs as eMAS (Figure 7), the AOD distributions are significantly different. When retrieval box resolution increases, the trend of each AOD distribution also differs, even for similar retrieval box size (e.g., ABI and eMAS 5 km resolution). When retrieval box size increases, the percentage of eMAS data falling within AOD  $< 0.3$  also increases, indicating an AOD distribution shift to smaller AOD. This shift is accompanied by a loss of high AODs (AOD  $> 2$ ) and a sharp decrease in the number of AOD retrievals between 0.5 and 0.7. This indicates a sharp plume boundary instead of a smooth transition. ABI AOD distributions peak at 0.3–0.4, which is much larger than the peak from the eMAS AOD distributions with resolution finer than 15 km. The difference is



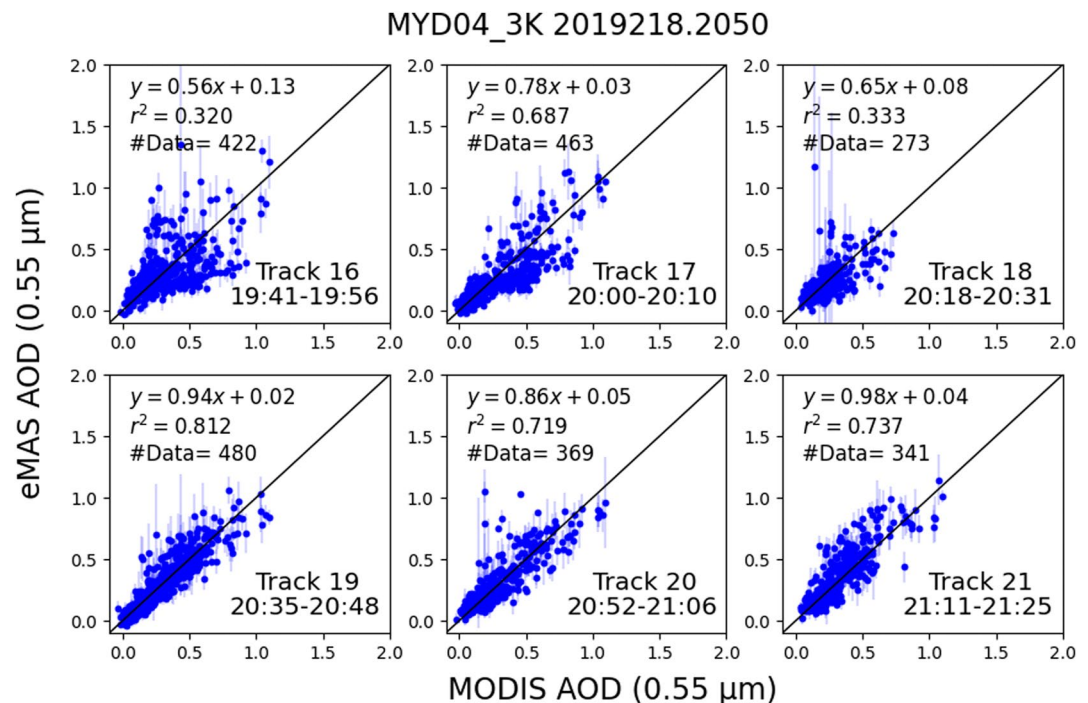


**Figure 9.** Comparisons between enhanced-MODIS Airborne Simulator (eMAS) and MODIS Aqua aerosol optical depth (AOD) on 6 August 2019, at 20:50 UTC. The eMAS data are from Flight number 19910 and track number 16–21. The standard deviation of collocated eMAS within MODIS one AOD grid is shown as blue bar. The black line is the one-to-one line and red line is the linear fit. Error statistics are shown in each panel.

partially caused by the general differences in ABI retrieval versus eMAS (Section 3.2; Figure 3). ABI data also have larger contribution from smaller value of AODs when compared to eMAS, especially for ABI 16.5 km ( $10 \times 10$ ) retrieval box data. Although AOD distribution at lower AOD end is different between from ABI and eMAS, ABI 5 km ( $3 \times 3$ ) data do show a smoother decreasing of AOD number toward higher value of AOD, which is similar to the pattern from finer eMAS resolution products. While ABI 16.5 km ( $10 \times 10$ ) data shows an AOD gap between 0.6 and 0.7, which matches what eMAS 15 km product is shown. These missing median value AOD can be an indicator that retrieval box spatial resolution is too coarse for a given plume.

Note that Figure 8 suggests an approximately log-normal distribution for smoke AOD within the depicted scene (Eck et al., 2001; N. Y. O'Neill et al., 2000; Sayer & Knobelspiesse, 2019; Sayer et al., 2020). While the number of pixels contained within the retrieval box are variable due to retrieval box resolution, some of these numbers are small (e.g., aggregating 4 pixels for eMAS 0.1 km resolution, 9 nominal pixels for ABI 5 km resolution). For a Gaussian distribution, the calculated mean should be unbiased for datapoints with limited number, however for a lognormal, we might expect it to be low biased (Povey & Grainger, 2018; Sayer & Knobelspiesse, 2019). The similar procedures applied to both eMAS and ABI, thus the bias does not impact our conclusion of spatial resolution, but rather reminds us that there is bias existing in retrieval products.

## 6. Capturing Temporal Change of Smoke Plume From Space

With its frequent temporal sampling, ABI may be able to characterize quickly changing fire emissions whereas MODIS and VIIRS cannot. With multiple tracks over a fire, eMAS can as well. In this section we use operational AOD product from MODIS, our smoke focused ABI and eMAS data sets to explore the temporal characteristics of the smoke. First, we compare retrieved AOD from multiple eMAS flight tracks of the Williams Flat fire on 6 August 2019, to the 3 km resolution operational AOD product from the MODIS Aqua granule at 20:50 UTC (Figure 9). In this way we can see the consequences of increasing separation in time between eMAS views and the MODIS granule. This granule is chosen because (a). There are six eMAS tracks in sequence observing the smoke plume with time separation of 9–62 min, (b) the plume is well-developed and wide enough to be somewhat



**Table 5**

*Table of Enhanced-MODIS Airborne Simulator (eMAS) Track Time and the Difference to MODIS Granule Observation Time*

eMAS track	#16	#17	#18	#19	#20	#21
Beginning time	19:41	20:00	20:18	20:35	20:52	21:11
Ending time	19:56	20:10	20:31	20:48	21:06	21:25
Difference to MODIS (min)	62	45	26	9	10	28

stable, (c) the MODIS Aqua flight track is right over the plume providing a clear nadir view. The six eMAS track are flight number 19910 track numbers 16 to 21. eMAS track time and time differences to MODIS passing time are listed in Table 5. Collocations between MODIS and eMAS is described in Section 3.2.

Qualitatively we can see the plume steadily propagating eastwards with no sudden change of wind speed or intensity of the plume (please see supplement ABI RGB Movie S1 on 6 August 2019). Quantitative comparisons between AOD retrieved by the smoke-focused algorithm applied to eMAS with those collocated spatially with standard DT MODIS AOD retrievals (Table 5) are shown in Figure 9. Here we plot values of individual retrieval boxes, not plume means or maximums. Agreement is good between eMAS and the MODIS retrievals for Tracks 19 to 21, time differences of 9–28 min. The discrepancies between satellite and eMAS become larger when time differences are greater than half hour to an hour. Of course, these time thresholds are solely dependent on the dynamics of the observed plume and can vary drastically between cases. However, it shows that for the Williams Flat Fire case, ABI with its 10-min temporal resolution should be able to characterize the plume and distinguish its time evolution, as long as the spatial resolution is sufficiently fine, as per Figure 7.

From the previous spatial and temporal analyses, we expect that a 3 km 10-min ABI product, should be sufficient to characterize the evolving Williams Flat fire plume. Figure 10 shows the time series of mean plume AOD using collocated eMAS smoke-focused AOD (red) and ABI 3 km smoke-focused AOD (blue) for the Williams Flat Fire on both 6 and 7 August 2019. The collocation criteria are the same as in Section 3.2. A small rectangular box is chosen between 47.8°N–48.3°N and 117.5°W–118.6°W to represent the smoke region. All AODs within this box are averaged and the number of paired data are shown by gray bars quantified by the right-hand axis.

We can see that the mean AOD time series from both ABI sensors follow the eMAS values as they evolve over time, except for ABI-16 at the beginning of the 6 August time series when the fire had just started. Even so both eMAS and ABI-E capture that puff of smoke at 19:20 UTC. The magnitude and variation of the ABI AODs generally agree with eMAS AODs. No obvious trend of AOD is observed on 6 August, but a slight decrease in plume intensity is found in the latter part of 7 August. The averaged AOD is greater than 0.4 for 6 August and 0.7 for 7 August, indicating stronger emission on the second day. Within one time stamp, the standard deviations from all three products are very large, indicating a wide distribution of AOD within the box, from an intense smoke plume to background aerosol loading. There is also little sudden change of AOD from time step to time step, indicating that observing this plume every 30 mins is adequate to capture its temporal variations. The snapshots of the averaged AOD over the defined plume area from standard DT MODIS Terra and Aqua 3 km product are lower than those from eMAS and ABI, indicating missing retrievals when it is very close to the emission sources. This is expected as the data is directly from operational products without algorithm tuning toward retrieving smoke.

## 7. Conclusions

The DT aerosol algorithm is modified and applied to the eMAS sensor data during the FIREX\_AQ campaign. eMAS DT standard products for the entire FIREX\_AQ campaign period are available and can be accessed via the FIREX\_AQ website. The DT eMAS product provide high spatial resolution (0.5 km) aerosol information. Validation and evaluation of the eMAS DT AOD at 0.55  $\mu\text{m}$  using AERONET and other DT satellite products including MODIS on Terra and Aqua, and ABI-16 and 17 on GOES-East and West suggests that the eMAS AOD falls within published expected error bars for the DT product. If the focus is on the plume region only, then the standard DT eMAS product captures most of the plume well especially for dispensed downwind smoke. There are some standard DT eMAS AOD data missing at the center of the optically dense plume when it is too close to the source region.

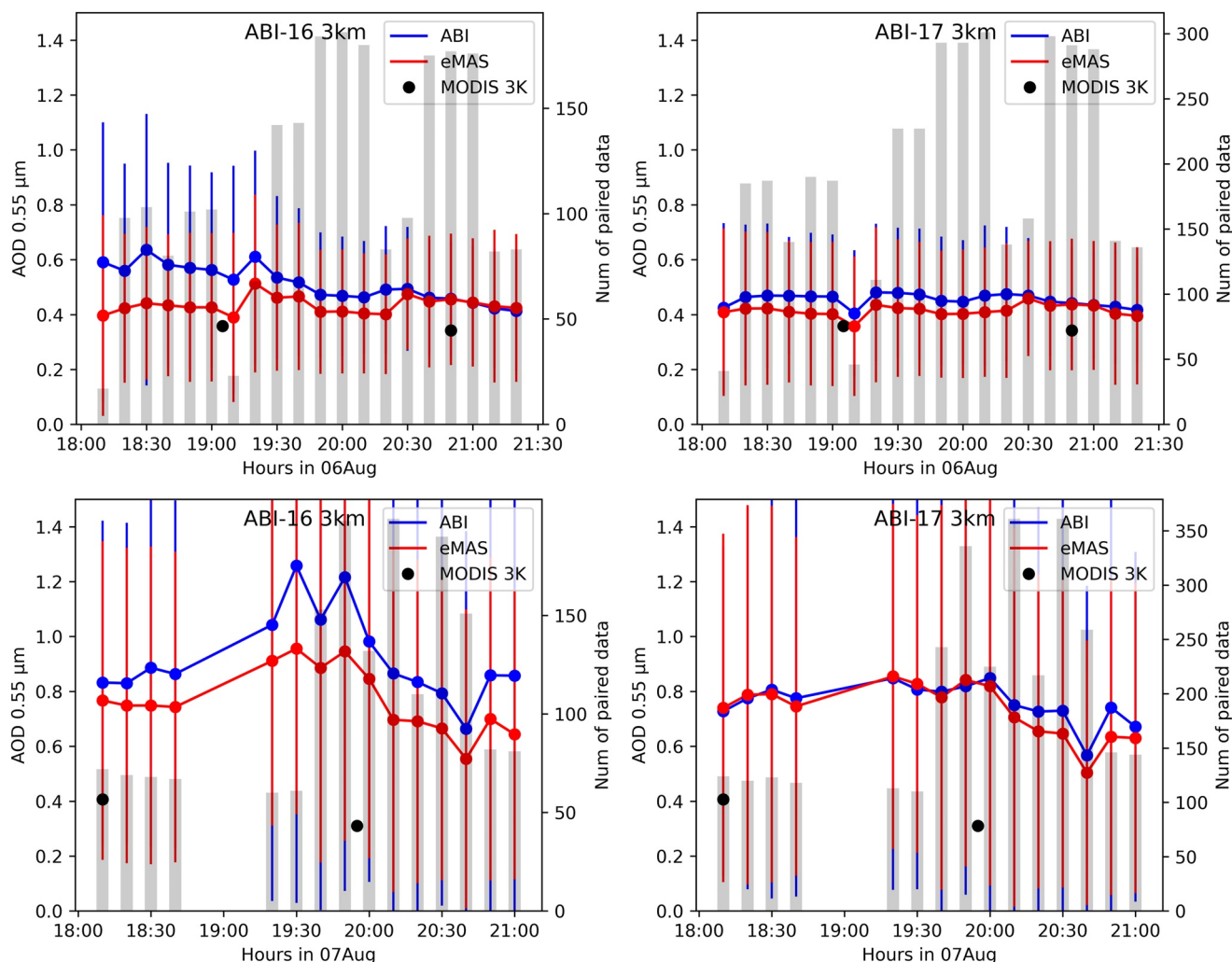


**Figure 10.** Aerosol optical depth (AOD) time series of the Williams Flat Fire on 6 August (top) and 7 August (bottom), 2019 from ABI-16 (left) and ABI-17 (right) 3 km smoke-focused products and enhanced-MODIS Airborne Simulator (eMAS) smoke-focused product. Collocated eMAS and Advanced Baseline Imager data are averaged within  $47.8^{\circ}\text{N}$ – $48.3^{\circ}\text{N}$  and  $117.5^{\circ}\text{W}$ – $118.6^{\circ}\text{W}$  to represent the smoke plume, respectively. The standard deviation represents the variation of AOD within the area. Number of collocated data for each time step is shown by the gray bars. The black dots are the averaged standard Dark Target (DT) MODIS Terra and Aqua AOD within the defined area. Differences between smoke-focused and standard DT algorithms are shown in Table 3.

With the aim to retrieve as much aerosol as possible near the fire emission sources, we modified the standard DT algorithm to create a smoke-focused product separately for eMAS and ABI by modifying the data pre-processing procedures. The modified filters include cloud masks and in-land water mask. The smoke-focused products provide much more smoke plume AOD than the standard DT products and still provide robust aerosol retrievals near the source region. Because of the relaxation of many protective filters, using the smoke-focused products outside of our handpicked smoke area will introduce artifacts from the surface and clouds. Thus, the smoke-focused products cannot be applied globally and shall be only used to evaluate the targeted plumes. The smoke-focused eMAS AOD products corresponding to flight tracks that contain smoke plumes near their source regions will be available via the DT website online.

To accommodate the needs of this study that addresses sampling bias from other satellite aerosol products over the plume region, we further relax masking thresholds used by the smoke-focused algorithm. This least restrictive algorithm includes more bright and dark pixels within each of retrieval box and is referred to as the experimental algorithm. This algorithm maximizes the ability to retrieve optically dense smoke but introduces cloud/surface artifacts and is only used in the analyses to understand the impact of spatial resolution of AOD product on plume propertie.

The two modified algorithms allow us to answer the question we posed in Section 1. Namely, is it possible for operational satellite sensors to properly characterize aerosol plumes, given their spatial and temporal limitations?

First, we find that the ABI sensor with nominal 1 km spatial resolution (1.7 km in our region of interest) can match the much finer resolution eMAS product in terms of mean plume AOD, as long as the grouping of the native resolution observations into retrieval boxes remains smaller than the width of the plume. Thus, a 5 km ( $3 \times 3$ ) satellite product can retrieve mean plume characteristics for plumes with widths greater than 5 km, but not those less wide. Even if nominal 1 km satellite sensors such as ABI can match plume mean AOD, they will underestimate the maximum AOD values of the plume. However, by grouping 1.7 km ABI data into standard 16.5 km ( $10 \times 10$ ) retrieval boxes, even the plume mean AOD will be underestimated for plumes with widths less than 16 km. This finding also suggests that for plume widths larger than 16 km, the standard DT satellite products will be able to capture the mean plume optical properties in our region of interest.

Second, we found that when the satellite product spatial resolution is coarser than the observed plume width, the retrieved plume mean AOD is not necessarily smaller than the true smoke plume intensity nor does it monotonically decrease with increasing retrieval box size. There are a range of retrieval box sizes that are slightly larger than the plume width where plume AOD fluctuates as the sensor rows align and misalign with the plume axis. Researchers shall be aware of this when using such satellite data to study/represent individual plumes. Creating a probability density function for AOD from retrievals in and around the plume may give some hints on whether the spatial resolution from satellite products is too coarse for target plumes.

Third, although experimental satellite product can represent the plume mean AOD, they capture very different AOD distributions than eMAS at 50-m resolution. Satellite data with 1 km native resolution, will systematically underestimate plume maximum AOD, which decreases exponentially with increasing retrieval resolution.

Fourth, as the impact of temporal resolution of aerosol products is solely dependent on the dynamics of the smoke, for the relatively steady Williams Flat Fire, we note that a temporal window of about 30 min was sufficient for MODIS AOD to match the AOD from the much more frequent overpasses of eMAS. This suggests that both ABI-16 and 17, measuring at 10-min intervals, should be able to characterize the temporal evolution of the smoke from this fire. Indeed, plotting collocated plume AOD time series as retrieved from both ABI sensors and eMAS on two consecutive days show that all sensors are capturing the general trends of this smoke.

Thus, this study suggests that while standard aerosol algorithms sometimes fail to characterize smoke plumes near their fire sources, especially for small plumes, because of the protective filtering required by a global product, this is not an inherent failing of the satellite sensors themselves. Algorithms can be adjusted to retrieve smoke near fires in a particular area and that a satellite sensor with actual 1.7 km spatial resolution and 10 to 30-min temporal resolution is adequate to characterize evolving aerosol plumes that are at least 5 km wide. With the correct spatial and temporal resolution applied to satellite observations, customized satellite products can capture the variation and intensity of moderate-scale fire emissions.

### Data Availability Statement

The aerosol product generated by the standard DT algorithm on the eMAS sensor during the entire FIREX\_AQ campaign is publicly available via the NASA LAADS website ([https://ladsweb.modaps.eosdis.nasa.gov/archive/MAS\\_eMAS/FIREXAQ/](https://ladsweb.modaps.eosdis.nasa.gov/archive/MAS_eMAS/FIREXAQ/)) and the FIREX\_AQ data archive (<https://www-air.larc.nasa.gov/cgi-bin/ArcView/firexaq?ER2=1#LEVY.ROBERT/>). Additionally, aerosol retrieval data from the smoke-focused algorithm over Williams Flat Fire events are available for studies that focuses on individual plumes. Due to the nature of this dataset, it is only available upon request. Please contact the corresponding author for inquiries regarding access to the smoke-focused aerosol data. AERONET data gathered during the FIREX\_AQ campaign can be downloaded at AERONET website (Holben et al., 2018) ([https://aeronet.gsfc.nasa.gov/new\\_web/DRAGON-FIREX-AQ\\_2019.html](https://aeronet.gsfc.nasa.gov/new_web/DRAGON-FIREX-AQ_2019.html)).

## Acknowledgments

We express our gratitude to the FIREX-AQ campaign, as well as the ER-2 and eMAS teams, for providing the invaluable eMAS data. We also extend our thanks to the AERONET team for providing ground measurements. We are grateful to NASA HQ, particularly Barry Lefer and the Tropospheric Composition Program (TCP), for their funding support for this research. Special thanks go to the FIREX\_AQ management team for their valuable assistance throughout the project. Additionally, we acknowledge the MEaSUREs (ROSES-2017) funding for the development of DT products on ABI.

## References

- Anderson, J. G., Dykema, J. A., Goody, R. M., Hu, H., & Kirk-Davidoff, D. B. (2004). Absolute, spectrally-resolved, thermal radiance: A benchmark for climate monitoring from space. *Journal of Quantitative Spectroscopy and Radiative Transfer*, 85(3–4), 367–383. [https://doi.org/10.1016/s0022-4073\(03\)00232-2](https://doi.org/10.1016/s0022-4073(03)00232-2)
- Brennan, J. I., Kaufman, Y. J., Koren, I., & Li, R. R. (2005). Aerosol-cloud interaction-misclassification of MODIS clouds in heavy aerosol. *IEEE Transactions on Geoscience and Remote Sensing*, 43(4), 911. <https://doi.org/10.1109/tgrs.2005.844662>
- Bruegge, C. J., Arnold, G. T., Czapla-Myers, J., Dominguez, R., Helmlinger, M. C., Thompson, D. R., et al. (2021). Vicarious calibration of eMAS, AirMSPI, and AVIRIS sensors during FIREX-AQ. *IEEE Transactions on Geoscience and Remote Sensing*, 59(12), 10286–10297. <https://doi.org/10.1109/tgrs.2021.3066997>
- Chin, M., Diehl, T., Tan, Q., Prospero, J. M., Kahn, R. A., Remer, L. A., et al. (2014). Multi-decadal aerosol variations from 1980 to 2009: A perspective from observations and a global model. *Atmospheric Chemistry and Physics*, 14(7), 3657–3690. <https://doi.org/10.5194/acp-14-3657-2014>
- Eck, T. F., Holben, B. N., Reid, J. S., Dubovik, O., Smirnov, A., O'Neill, N. T., et al. (1999). Wavelength dependence of the optical depth of biomass burning, urban, and desert dust aerosols. *Journal of Geophysical Research*, 104(D24), 31333–31349.
- Eck, T. F., Holben, B. N., Ward, D. E., Dubovik, O., Reid, J. S., Smirnov, A., et al. (2001). Characterization of the optical properties of biomass burning aerosols in Zambia during the 1997 ZIBBEE field campaign. *Journal of Geophysical Research*, 106(D4), 3425–3448. <https://doi.org/10.1029/2000jd900555>
- Freeborn, P. H., Wooster, M. J., & Roberts, G. (2011). Addressing the spatiotemporal sampling design of MODIS to provide estimates of the fire radiative energy emitted from Africa. *Remote Sensing of Environment*, 115(2), 475–489. <https://doi.org/10.1016/j.rse.2010.09.017>
- Gupta, P., Levy, R. C., Mattoo, S., Remer, L. A., Holz, R. E., & Heidinger, A. K. (2019). Applying the dark target aerosol algorithm with advanced Himawari imager observations during the KORUS-AQ field campaign. *Atmospheric Measurement Techniques*, 12(12), 6557–6577. <https://doi.org/10.5194/amt-12-6557-2019>
- Gupta, P., Levy, R. C., Mattoo, S., Remer, L. A., & Munchak, L. A. (2016). A surface reflectance scheme for retrieving aerosol optical depth over urban surfaces in MODIS Dark Target retrieval algorithm. *Atmospheric Measurement Techniques*, 9(7), 3293–3308. <https://doi.org/10.5194/amt-9-3293-2016>
- Gupta, P., Remer, L. A., Levy, R. C., & Mattoo, S. (2018). Validation of MODIS 3 km land aerosol optical depth from NASA's EOS Terra and Aqua missions. *Atmospheric Measurement Techniques*, 11(5), 3145–3159. <https://doi.org/10.5194/amt-11-3145-2018>
- Hodzic, A., Kasibhatla, P. S., Jo, D. S., Cappa, C. D., Jimenez, J. L., Madronich, S., & Park, R. J. (2016). Rethinking the global secondary organic aerosol (SOA) budget: Stronger production, faster removal, shorter lifetime. *Atmospheric Chemistry and Physics*, 16(12), 7917–7941. <https://doi.org/10.5194/acp-16-7917-2016>
- Holben, B. N., Kim, J., Sano, I., Mukai, S., Eck, T. F., Giles, D. M., et al. (2018). An overview of mesoscale aerosol processes, comparisons, and validation studies from DRAGON networks. *Atmospheric Chemistry and Physics*, 18(2), 655–671. <https://doi.org/10.5194/acp-18-655-2018>
- Huang, J., Laszlo, I., Lorraine, A., Liu, H., Zhang, H., Ciren, P., & Kondragunta, S. (2018). Screening for snow/snowmelt in SNPP VIIRS aerosol optical depth algorithm. *Atmospheric Measurement Techniques*, 11(10), 5813–5825. <https://doi.org/10.5194/amt-11-5813-2018>
- Hyer, E. J., Reid, J. S., & Zhang, J. (2011). An over-land aerosol optical depth data set for data assimilation by filtering, correction, and aggregation of MODIS Collection 5 optical depth retrievals. *Atmospheric Measurement Techniques*, 4(3), 379–408. <https://doi.org/10.5194/amt-4-379-2011>
- Ichoku, C., Kaufman, Y. J., Giglio, L., Li, Z., Fraser, R. H., Jin, J. Z., & Park, W. M. (2003). Comparative analysis of daytime fire detection algorithms using AVHRR data for the 1995 fire season in Canada: Perspective for MODIS. *International Journal of Remote Sensing*, 24(8), 1669–1690. <https://doi.org/10.1080/01431160210144697>
- Jungheun Noyes, K. T., Kahn, R. A., Limbacher, J. A., Li, Z., Fenn, M. A., Giles, D. M., et al. (2020). Wildfire smoke particle properties and evolution, from space-based multi-angle imaging II: The Williams Flats Fire during the FIREX-AQ Campaign. *Remote Sensing*, 12(22), 3823. <https://doi.org/10.3390/rs12223823>
- Kaufman, Y. J., Hobbs, P. V., Kirchhoff, V. W. J. H., Artaxo, P., Remer, L. A., Holben, B. N., et al. (1998). Smoke, clouds, and radiation-Brazil (SCAR-B) experiment. *Journal of Geophysical Research*, 103(D24), 31783–31808. <https://doi.org/10.1029/98jd02281>
- Kaufman, Y. J., Ichoku, C., Giglio, L., Korontzi, S., Chu, D. A., Hao, W. M., et al. (2003). Fire and smoke observed from the Earth Observing System MODIS instrument—Products, validation, and operational use. *International Journal of Remote Sensing*, 24(8), 1765–1781. <https://doi.org/10.1080/01431160210144741>
- Kaufman, Y. J., Kleidman, R. G., & King, M. D. (1998). SCAR-B fires in the tropics: Properties and remote sensing from EOS-MODIS. *Journal of Geophysical Research*, 103(D24), 31955–31968. <https://doi.org/10.1029/98jd02460>
- Kaufman, Y. J., Setzer, A., Ward, D., Tanre, D., Holben, B. N., Menzel, P., et al. (1992). Biomass burning airborne and spaceborne experiment in the Amazonas (BASE-A). *Journal of Geophysical Research*, 97(D13), 14581–14599. <https://doi.org/10.1029/92jd00275>
- Koren, I., Feingold, G., & Remer, L. A. (2010). The invigoration of deep convective clouds over the Atlantic: Aerosol effect, meteorology or retrieval artifact? *Atmospheric Chemistry and Physics*, 10(18), 8855–8872. <https://doi.org/10.5194/acp-10-8855-2010>
- Kristiansen, N. I., Stohl, A., Olivè, D. J. L., Croft, B., Søvde, O. A., Klein, H., et al. (2016). Evaluation of observed and modelled aerosol lifetimes using radioactive tracers of opportunity and an ensemble of 19 global models. *Atmospheric Chemistry and Physics*, 16(5), 3525–3561. <https://doi.org/10.5194/acp-16-3525-2016>
- Kumar, A., Pierce, R. B., Ahmadv, R., Pereira, G., Freitas, S., Grell, G., et al. (2022). Simulating wildfire emissions and plume rise using geostationary satellite fire radiative power measurements: A case study of the 2019 Williams flats fire. *Atmospheric Chemistry and Physics*, 22(15), 10195–10219. <https://doi.org/10.5194/acp-22-10195-2022>
- Lennartson, E. M., Wang, J., Gu, J., Castro Garcia, L., Ge, C., Gao, M., et al. (2018). Diurnal variation of aerosol optical depth and PM 2.5 in South Korea: A synthesis from AERONET, satellite (GOCI), KORUS-AQ observation, and the WRF-chem model. *Atmospheric Chemistry and Physics*, 18(20), 15125–15144. <https://doi.org/10.5194/acp-18-15125-2018>
- Levy, R. C., Mattoo, S., Munchak, L. A., Remer, L. A., Sayer, A. M., Patadia, F., & Hsu, N. C. (2013). The Collection 6 MODIS aerosol products over land and ocean. *Atmospheric Measurement Techniques*, 6(11), 2989–3034. <https://doi.org/10.5194/amt-6-2989-2013>
- Levy, R. C., Mattoo, S., Sawyer, V., Shi, Y., Colarco, P. R., Lyapustin, A. I., et al. (2018). Exploring systematic offsets between aerosol products from the two MODIS sensors. *Atmospheric Measurement Techniques*, 11(7), 4073–4092. <https://doi.org/10.5194/amt-11-4073-2018>
- Levy, R. C., Remer, L. A., Kleidman, R. G., Mattoo, S., Ichoku, C., Kahn, R., & Eck, T. F. (2010). Global evaluation of the Collection 5 MODIS dark-target aerosol products over land. *Atmospheric Chemistry and Physics*, 10(21), 10399–10420. <https://doi.org/10.5194/acp-10-10399-2010>
- Liu, X., & Zeng, Z. C. (2019). Mapping diurnal aerosol properties in east Asia from deep space climate observatory. In *IGARSS 2019–2019 IEEE International Geoscience and remote sensing symposium* (pp. 7606–7609). IEEE.



- Manoj, M. G., Devara, P. C. S., Safai, P. D., & Goswami, B. N. (2011). Absorbing aerosols facilitate transition of Indian monsoon breaks to active spells. *Climate Dynamics*, 37(11–12), 2181–2198. <https://doi.org/10.1007/s00382-010-0971-3>
- Martins, J. V., Tanré, D., Remer, L., Kaufman, Y., Mattoo, S., & Levy, R. (2002). MODIS cloud screening for remote sensing of aerosols over oceans using spatial variability. *Geophysical Research Letters*, 29(12), MOD4-1. <https://doi.org/10.1029/2001gl013252>
- O’Neil, N. Y., Ignatov, A., Holben, B. N., & Eck, T. F. (2000). The lognormal distribution as a reference for reporting aerosol optical depth statistics; Empirical tests using multi-year, multi-site AERONET Sunphotometer data. *Geophysical Research Letters*, 27(20), 3333–3336. <https://doi.org/10.1029/2000gl011581>
- O’Neill, N. T., Dubovik, O., & Eck, T. F. (2001). Modified Ångström exponent for the characterization of submicrometer aerosols. *Applied Optics*, 40(15), 2368–2375. <https://doi.org/10.1364/ao.40.002368>
- O’Neill, N. T., Eck, T. F., Smirnov, A., Holben, B. N., & Thulasiraman, S. (2003). Spectral discrimination of coarse and fine mode optical depth. *Journal of Geophysical Research*, 108(D17), 4559. <https://doi.org/10.1029/2002jd002975>
- Ortega, A. M., Day, D. A., Cubison, M. J., Brune, W. H., Bon, D., De Gouw, J. A., & Jimenez, J. L. (2013). Secondary organic aerosol formation and primary organic aerosol oxidation from biomass-burning smoke in a flow reactor during FLAME-3. *Atmospheric Chemistry and Physics*, 13(22), 11551–11571. <https://doi.org/10.5194/acp-13-11551-2013>
- Peterson, D., Wang, J., Ichoku, C., Hyer, E., & Ambrosia, V. (2013). A sub-pixel-based calculate of fire radiative power from MODIS observations: 1. Algorithm development and validation. *Remote Sensing of Environment*, 129, 262–279. <https://doi.org/10.1016/j.rse.2012.10.036>
- Platnick, S., King, M. D., Ackerman, S. A., Paul Menzel, W., Baum, B. A., Riédi, J. C., & Frey, R. A. (2003). The MODIS cloud products: Algorithms and examples from Terra. *IEEE Transactions on Geoscience and Remote Sensing*, 41(2), 459–473. <https://doi.org/10.1109/tgrs.2002.808301>
- Povey, A. C., & Grainger, R. G. (2018). Toward more representative gridded satellite products. *IEEE Geoscience and Remote Sensing Letters*, 16(5), 672–676. <https://doi.org/10.1109/lgrs.2018.2881762>
- Ramanathan, V., Ramana, M. V., Roberts, G., Kim, D., Corrigan, C., Chung, C., & Winker, D. (2007). Warming trends in Asia amplified by brown cloud solar absorption. *Nature*, 448(7153), 575–578. <https://doi.org/10.1038/nature06019>
- Reid, J. S., Koppmann, R., Eck, T. F., & Eleuterio, D. P. (2005). A review of biomass burning emissions part II: Intensive physical properties of biomass burning particles. *Atmospheric Chemistry and Physics*, 5(3), 799–825. <https://doi.org/10.5194/acp-5-799-2005>
- Remer, L. A., Kaufman, Y. J., Tanré, D., Mattoo, S., Chu, D. A., Martins, J. V., et al. (2005). The MODIS aerosol algorithm, products and validation. *Journal of the Atmospheric Sciences*, 62(4), 947–973. <https://doi.org/10.1175/jas3385.1>
- Remer, L. A., Mattoo, S., Levy, R. C., Heidinger, A., Pierce, R. B., & Chin, M. (2012). Retrieving aerosol in a cloudy environment: Aerosol product availability as a function of spatial resolution. *Atmospheric Measurement Techniques*, 5(7), 1823–1840. <https://doi.org/10.5194/amt-5-1823-2012>
- Roberts, G., Wooster, M., & Lagoudakis, E. (2009). Annual and diurnal African biomass burning temporal dynamics. *Biogeosciences*, 6(5), 849–866. <https://doi.org/10.5194/bg-6-849-2009>
- San-Miguel-Ayán, J., & Ravail, N. (2005). Active fire detection for fire emergency management: Potential and limitations for the operational use of remote sensing. *Natural Hazards*, 35(3), 361–376. <https://doi.org/10.1007/s11069-004-1797-2>
- Sano, I., Mukai, S., Nakata, M., & Holben, B. N. (2016). Regional and local variations in atmospheric aerosols using ground-based sun photometry during Distributed Regional Aerosol Gridded Observation Networks (DRAGON) in 2012. *Atmospheric Chemistry and Physics*, 16(22), 14795–14803. <https://doi.org/10.5194/acp-16-14795-2016>
- Sayer, A. M., Govaerts, Y., Kolmonen, P., Lipponen, A., Luffarelli, M., Mielonen, T., et al. (2020). A review and framework for the evaluation of pixel-level uncertainty estimates in satellite aerosol remote sensing. *Atmospheric Measurement Techniques*, 13(2), 373–404. <https://doi.org/10.5194/amt-13-373-2020>
- Sayer, A. M., & Knobelspiesse, K. D. (2019). How should we aggregate data? Methods accounting for the numerical distributions, with an assessment of aerosol optical depth. *Atmospheric Chemistry and Physics*, 19(23), 15023–15048. <https://doi.org/10.5194/acp-19-15023-2019>
- Schmit, T. J., Gunshor, M. M., Menzel, W. P., Gurka, J. J., Li, J., & Bachmeier, A. S. (2005). Introducing the next-generation advanced baseline imager on GOES-R. *Bulletin of the American Meteorological Society*, 86(8), 1079–1096. <https://doi.org/10.1175/bams-86-8-1079>
- Schmit, T. J., Lindstrom, S. S., Gerth, J. J., & Gunshor, M. M. (2018). Applications of the 16 spectral bands on the advanced baseline imager (ABI).
- Shi, Y., Levy, R., Remer, L., Mattoo, S., Gupta, P., Sawyer, V., & Zhang, Z. (2021). Evaluating aerosol retrievals from LEO and GEO orbits: A step towards consistent global aerosol data records. In *AGU fall meeting 2021, held in New Orleans, LA, 13-17 December 2021b*, id. A45P-2061.
- Shi, Y., Zhang, J., Reid, J. S., Holben, B., Hyer, E. J., & Curtis, C. (2011). An analysis of the collection 5 MODIS over-ocean aerosol optical depth product for its implication in aerosol assimilation. *Atmospheric Chemistry and Physics*, 11(2), 557–565. <https://doi.org/10.5194/acp-11-557-2011>
- Shi, Y. R., Levy, R. C., Eck, T. F., Fisher, B., Mattoo, S., Remer, L. A., et al. (2019). Characterizing the 2015 Indonesia fire event using modified MODIS aerosol retrievals. *Atmospheric Chemistry and Physics*, 19(1), 259–274. <https://doi.org/10.5194/acp-19-259-2019>
- Shi, Y. R., Levy, R. C., Yang, L., Remer, L. A., Mattoo, S., & Dubovik, O. (2021). A dark target research aerosol algorithm for MODIS observations over eastern China: Increasing coverage while maintaining accuracy at high aerosol loading. *Atmospheric Measurement Techniques*, 14(5), 3449–3468. <https://doi.org/10.5194/amt-14-3449-2021>
- Shinozuka, Y., & Redemann, J. (2011). Horizontal variability of aerosol optical depth observed during the ARCTAS airborne experiment. *Atmospheric Chemistry and Physics*, 11(16), 8489–8495. <https://doi.org/10.5194/acp-11-8489-2011>
- Spencer, R. S., Levy, R. C., Remer, L. A., Mattoo, S., Arnold, G. T., Hlavka, D. L., et al. (2019). Exploring aerosols near clouds with high-spatial-resolution aircraft remote sensing during SEAC4RS. *Journal of Geophysical Research: Atmospheres*, 124(4), 2148–2173. <https://doi.org/10.1029/2018jd028989>
- Van Donkelaar, A., Martin, R. V., Brauer, M., & Boys, B. L. (2015). Use of satellite observations for long-term exposure assessment of global concentrations of fine particulate matter. *Environmental Health Perspectives*, 123(2), 135–143. <https://doi.org/10.1289/ehp.1408646>
- Wang, J., Yue, Y., Wang, Y., Ichoku, C., Ellison, L., & Zeng, J. (2018). Mitigating satellite-based fire sampling limitations in deriving biomass burning emission rates: Application to WRF-chem model over the Northern Sub-Saharan African region. *Journal of Geophysical Research: Atmospheres*, 123(1), 507–528. <https://doi.org/10.1002/2017jd026840>
- Warneke, C., Schwarz, J. P., Dibb, J., Kalashnikova, O., Frost, G., Al-Saad, J., et al. (2023). Fire influence on regional to global Environments and air quality (FIREX-AQ). *Journal of Geophysical Research: Atmospheres*, 128(2), e2022JD037758. <https://doi.org/10.1029/2022jd037758>
- Wiggins, E. B., Soja, A. J., Gargulinski, E., Halliday, H. S., Pierce, R. B., Schmidt, C. C., et al. (2020). High temporal resolution satellite observations of fire radiative power reveal link between fire behavior and aerosol and gas emissions. *Geophysical Research Letters*, 47(23), e2020GL090707. <https://doi.org/10.1029/2020gl090707>



- Williamson, G. J., Price, O. F., Henderson, S. B., & Bowman, D. M. (2012). Satellite-based comparison of fire intensity and smoke plumes from prescribed fires and wildfires in south-eastern Australia. *International Journal of Wildland Fire*, 22(2), 121–129. <https://doi.org/10.1071/wf11165>
- Ye, X., Arab, P., Ahmadov, R., James, E., Grell, G. A., Pierce, B., et al. (2021). Evaluation and intercomparison of wildfire smoke forecasts from multiple modeling systems for the 2019 Williams Flats fire. *Atmospheric Chemistry and Physics*, 21(18), 14427–14469. <https://doi.org/10.5194/acp-21-14427-2021>
- Yokelson, R. J., Crounse, J. D., DeCarlo, P. F., Karl, T., Urbanski, S., Campos, T., et al. (2009). Emissions from biomass burning in the Yucatan. *Atmospheric Chemistry and Physics*, 9(15), 5785–5812. <https://doi.org/10.5194/acp-9-5785-2009>
- Yu, H., Remer, L. A., Chin, M., Bian, H., Kleidman, R. G., & Diehl, T. (2008). A satellite-based assessment of transpacific transport of pollution aerosol. *Journal of Geophysical Research*, 113(D14), D14S12. <https://doi.org/10.1029/2007jd009349>
- Yu, H., Yang, Y., Wang, H., Tan, Q., Chin, M., Levy, R. C., et al. (2020). Interannual variability and trends of combustion aerosol and dust in major continental outflows revealed by MODIS retrievals and CAM5 simulations during 2003–2017. *Atmospheric Chemistry and Physics*, 20(1), 139–161. <https://doi.org/10.5194/acp-20-139-2020>
- Yuan, T., Remer, L. A., Pickering, K. E., & Yu, H. (2011). Observational evidence of aerosol enhancement of lightning activity and convective invigoration. *Geophysical Research Letters*, 38(4). <https://doi.org/10.1029/2010gl046052>